



19 **Abstract**

20 Atmospheric particles can impact cloud formation and play a critical role in regulating  
21 cloud properties. However, particle characteristics at the single particle level and their  
22 ability to act as ice nucleating particles (INPs) over the marine atmosphere are poorly  
23 understood. In this study, we present micro-spectroscopic characterizations and ice  
24 nucleation properties of particles collected during a cruise from South Korea to  
25 Antarctica in 2019. Most of the samples were dominated by fresh sea salt, aged sea salt,  
26 and sea salt mixed with sulfate particles, with total number percentages ranging from  
27 48% to 99% over the Western Pacific and the Southern Ocean. The mixing state index  
28 of the particle population ranged from 50% to 95% over the northern and southern  
29 hemispheres. Multiphase processes on sea salt particles resulted in chlorine deficiency.  
30 This selective aging process made the marine particle population more externally mixed.  
31 Ice nucleation onset conditions primarily for the deposition mode were measured and  
32 the investigated particles showed diverse ice nucleation abilities. The fresh sea salt  
33 particles with organic coatings exhibited the highest ice nucleation ability at a relative  
34 humidity with respect to ice as low as 121%. The sea salt mixed sulfate particle was  
35 enriched in INPs by a factor of 1.9. Aging processes affected both particles' mixing  
36 state and their ice nucleation abilities. Our analysis shows that assuming an internally  
37 mixed particle population in the marine atmosphere can lead to errors of several orders  
38 of magnitude in predicting ice nucleation rates.

39

40

41 **Keywords:** Ice nucleation, ice nucleating particles, single particle analysis, marine  
42 aerosols, elemental composition, mixing state

## 43 **1. Introduction**

44 As 70.8% of the Earth's surface is covered by oceans, marine aerosol particles are one  
45 of the most important types of natural aerosols in the global inventory (Myriokefalitakis  
46 et al., 2010; De Leeuw et al., 2011). Aerosols in marine environments can affect the  
47 ocean biogeochemical cycles and indirectly or directly affect Earth system's radiation  
48 budget (Song et al., 2022). The sixth Intergovernmental Panel on Climate Change  
49 (IPCC) assessment report highlights a significant uncertainty in predicting the net  
50 effective radiative forcing of aerosols, with aerosol-cloud interactions contributing the  
51 most (IPCC, 2021). The impacts of atmospheric particles on cloud microphysical  
52 processes are still poorly understood. The physicochemical properties of particles  
53 determine their abilities to serve as cloud condensation nuclei (CCN) and ice nucleating  
54 particles (INPs), thereby affecting cloud microphysical processes. Particles serving as  
55 INPs can potentially trigger ice nucleation via four pathways: (1) deposition ice  
56 nucleation (DIN), which forms ice by the direct deposition of water vapor onto particle  
57 surface; (2) immersion freezing (IMF), which droplet freezing is triggered by immersed  
58 particles; (3) contact freezing, when supercooled droplets freeze by the contact with  
59 particles; (4) condensation freezing, when droplets freeze as water vapor condenses on  
60 droplets or particles at temperatures below 0 °C. The majority of recent studies have  
61 focused on the IMF and DIN under mixed-phase and ice cloud conditions (Hoose and  
62 Möhler, 2012; Murray et al., 2012; Kanji et al., 2017; Knopf et al., 2018).

63  
64 Diverse sources and atmospheric processes bring great challenges to the study of the  
65 physicochemical properties of marine particles. One of the major particle types in the  
66 marine atmosphere is sea spray aerosol (SSA) generated from wave breaking and  
67 bubble bursting over the ocean surface. Their compositions are mainly affected by  
68 seawater, sea ice, and biological activities and have minimum influence from  
69 anthropogenic activities (Kunwar et al., 2023). Other sources may also contribute to  
70 marine aerosols, such as ship emission (Ault et al., 2009, 2010) and long-range transport  
71 of aerosols from industrial emission, biomass burning, dust storms, and fossil fuel

72 combustion (Han et al., 2006; Fu et al., 2013; Geng et al., 2019). In addition,  
73 atmospheric oxidation of volatile organic compounds from the ocean or anthropogenic  
74 activities results in gas-particle conversion, multiphase reactions, and the formation of  
75 secondary materials on particles (Cochran et al., 2017). For example, dimethyl sulfide  
76 (DMS) from marine sources can be oxidized to form methanesulfonic acid (MSA) and  
77 sulfuric acid ( $\text{H}_2\text{SO}_4$ ) in the atmosphere (Barnes et al., 2006; Chen et al., 2018; Berndt  
78 et al., 2023). Moreover, multiphase reactions can occur on the surface or within particles  
79 causing changes in their physicochemical properties of particles (Cochran et al., 2017).  
80 The oxidation products of DMS ( $\text{H}_2\text{SO}_4$  and MSA) can react with sea salt particles  
81 resulting in chloride depletion from acid displacements (Liu et al., 2011).

82

83 Due to their diverse sources and dynamic evolution in the atmosphere, individual  
84 particles become a mixture of various compositions and have complex morphologies  
85 (Riemer et al., 2019; Li et al., 2016). Chemical mixing state is a term used to describe  
86 how various chemical species are mixed within individual particles in an aerosol  
87 population (Riemer and West, 2013). Quantifying the chemical mixing state helps us to  
88 discuss how the population with different internal or external mixing affects its optical  
89 properties, cloud formation properties, and climatic impacts (Cziczo et al., 2017; Kanji  
90 et al., 2017; Knopf et al., 2018; Riemer et al., 2019; Burrows et al., 2022). Previous  
91 studies have quantified the chemical mixing state of an aerosol population using the  
92 mixing state index ( $\chi$ ), which is based on the mass percentages of various chemical  
93 species in single particles within a population (Riemer et al., 2019). Thus, chemical  
94 characteristics of individual particles should be achieved by single-particle techniques  
95 to quantify  $\chi$ . Previous studies have focused on mixing states including but not limited  
96 to marine particles (Ault et al., 2010; Park et al., 2014; Tomlin et al., 2021), biomass  
97 burning aerosol (BBA) (Tomlin et al., 2022; Healy et al., 2013), and dust particles  
98 (Fraund et al., 2017; Adachi et al., 2020). However, the impacts of particle sources and  
99 atmospheric aging on the chemical mixing state of marine particles are not well  
100 understood.

101

102 Laboratory and field studies have shown that various particle types have potential  
103 impacts on ice crystal formation in marine atmosphere. Natural INPs include mineral  
104 dust, soil particles, volcanic ash, SSA, BBA, and bioaerosols. Anthropogenic INPs  
105 include agricultural particles, metals and metal oxides from industrial processes, and  
106 fossil fuel combustion particles (Hoose and Möhler, 2012; Murray et al., 2012; Kanji  
107 et al., 2017). Laboratory studies have shown that SSA, marine phytoplankton, and  
108 related organics can server as INPs for both IMF and DIN (e.g. Knopf et al., 2011;  
109 Prather et al., 2013; Wilson et al., 2015; McCluskey et al., 2017; Schill and Tolbert,  
110 2014; Wagner et al., 2018). SSA can be efficient INPs via IMF before complete  
111 deliquescence (Schill and Tolbert, 2014). Wagner et al. (2018) showed that SSA and  
112 desert dust particles have similar ice nucleation active surface site density ( $n_s$ ) for DIN.  
113 Previous studies have also shown that  $n_s$  for SSA is 2-3 orders of magnitude lower than  
114 that for dust particles for IMF (DeMott et al., 2016; McCluskey et al., 2018a; Cornwell  
115 et al., 2019). Knopf et al. (2011) confirmed that intact cells or fragments of marine  
116 diatoms can act as INPs. Wilson et al. (2015) demonstrated that the sea surface  
117 microlayer is enriched with ice nucleating materials. McCluskey et al. (2018b)  
118 identified two types of INPs from mesocosm experiments, which were dissolved  
119 organic carbon coated particles and particles like intact cells or cell fragments from  
120 microorganisms.

121

122 Most of the field investigations over oceans have focused on the INP concentration  
123 measurements for IMF and at mixed-phase cloud conditions with relatively warmer  
124 temperatures (Bigg, 1973; Rosinski et al., 1995; DeMott et al., 2016; Mason et al., 2015;  
125 McCluskey et al., 2018b; Welti et al., 2018, 2020; Ladino et al., 2019). For example,  
126 Welti et al. (2020) found that INP concentration from ship-based measurements over  
127 the oceans were 1 to 2 orders of magnitude lower than continental observations. INP  
128 concentrations were lowest in the polar regions and highest in the temperate climate  
129 ocean at about 258 K (Welti et al., 2020). Inoue et al. (2021) found high INP  
130 concentrations under high wave conditions which were related to the release of organic  
131 carbon from the ocean. Studies also found that active INPs via IMF are likely biological

132 particles (e.g. Hartmann et al., 2020; McCluskey et al., 2018b; Gong et al., 2020).

133

134 There are several marine related field studies focusing on DIN and INP identification  
135 (e.g., Ladino et al., 2016; China et al., 2017; Alpert et al., 2022; Knopf et al., 2022,  
136 2023) . Alpert et al. (2022) confirmed that INPs in the ambient and laboratory-generated  
137 SSA were the sea salt with organic matter, which were exudates released from  
138 planktonic microorganisms. Over the Northeast Pacific Ocean, Knopf et al. (2022, 2023)  
139 found different ice nucleation abilities between daytime and nighttime particles in  
140 marine boundary layer and between particles in the free troposphere and that in marine  
141 boundary layer. Recent field studies have used advanced micro-spectroscopes and mass  
142 spectrometry to image and characterize the INPs and ice crystal residuals to understand  
143 their nature (e.g., Cziczo et al., 2017; Knopf et al., 2018). INPs and ice residuals are  
144 often mixtures of chemical species. Ice nucleation is inherently related to the mixing  
145 state of particles because it depends on the particle surface properties. Quantifying the  
146 ice nucleation rate also depends on the composition, surface area, and the mixing state  
147 of the particle population. The importance of mixing state for INPs is well recognized,  
148 but there are limited studies focusing on its quantification which is poorly understood  
149 (Kanji et al., 2017; Knopf et al., 2018; Riemer et al., 2019).

150

151 In this study, our main objectives are to quantify the mixing state and ice nucleation  
152 ability of marine particles over the Western Pacific and Southern Ocean. We quantify  
153 ice formation potential and elemental composition of particles over coastal and open  
154 oceans using microscope-based ice nucleation instrumentation and computer-  
155 controlled scanning electron microscopy with energy dispersive X-ray spectroscopy  
156 (CCSEM/EDX), respectively. The mixing state of particle population based on the  
157 elemental composition is derived for 29 marine ambient particle populations extending  
158 from the northern to the southern hemisphere. We measure the ice nucleation onset  
159 conditions and identify the nucleation pathways (DIN or IMF) for representative  
160 samples. In this study, we focus primarily on DIN and in some cases IMF below 240 K.  
161 Individual identified INPs are characterized and compared with the particle population

162 to relate ice nucleation ability to the mixing state. Potential errors in predicting ice  
163 nucleation rate are briefly discussed if models assume an internally mixed population.  
164 We perform ice nucleation kinetic analysis based on the experimental data and provide  
165 parameterizations for cloud modeling.

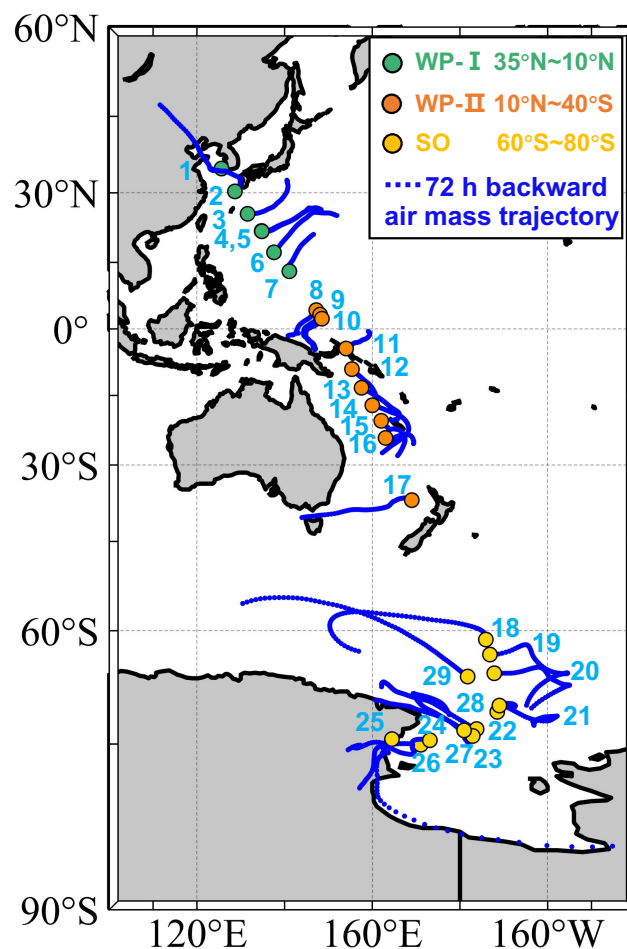
166

## 167 **2. Experimental methods**

### 168 **2.1 Particle sampling**

169 Aerosol particles were collected by a four-stage cascade impactor (SKC, Inc.) at a  
170 sample flow of  $9 \text{ L min}^{-1}$  on board the Korean ice breaker R/V *Araon* from October 31<sup>st</sup>  
171 to December 12<sup>nd</sup> in 2019. Particles were collected on the third and fourth stages of the  
172 impactor with 50% collection efficiency at aerodynamic sizes of  $0.5 \mu\text{m}$  and  $0.25 \mu\text{m}$ ,  
173 respectively. The inlet was located on the third deck of the ship at about 13 m above sea  
174 surface level (Park et al., 2020). As shown in Fig. 1, the cruise crossed about 110  
175 degrees of latitude from the Western Pacific near South Korea ( $34.93^\circ\text{N}$ ) to the Ross  
176 Sea in the Southern Ocean ( $75.12^\circ\text{S}$ ). Samples were collected on transmission electron  
177 microscopy (TEM) copper grids (Carbon Type-B, Ted Pella, Inc.) for single particle  
178 analysis by CCSEM/EDX and silicon wafer chips (Silson, Ltd.) with the hydrophobic  
179 coating ( $\text{Si}_3\text{N}_4$ ) for ice nucleation experiments following our previous studies (Wang et  
180 al., 2012a, 2016a; Knopf et al., 2014). Particles were collected simultaneously on these  
181 two substrates which were placed side by side in the same impactor. Particle samples  
182 were stored at room temperature in an airtight container with desiccant until analysis.  
183 This study primarily focuses on DIN at low temperatures and INP identification.  
184 Particles with a smaller size range may have a longer lifetime and can potentially be  
185 transported to higher altitudes in the atmosphere. Therefore, we limited our analysis to  
186 the samples collected on the fourth stage. Meteorological conditions and black carbon  
187 concentrations were measured by the onboard weather station and an aethalometer  
188 (AE22, Magee Scientific Co., USA), respectively. When the relative wind direction  
189 against the ship heading is between  $110^\circ$  and  $260^\circ$  and the relative wind speed is below  
190  $2 \text{ m s}^{-1}$ , samples may have been influenced by the ship exhaust (Park et al., 2020).

191 Potentially contaminated samples were excluded from the analysis, resulting in a total  
192 of 29 selected samples. The sampling location and 72 h backward air mass trajectories  
193 are shown in Fig. 1. Backward air mass trajectories were computed using the Hybrid  
194 Single-Particle Lagrangian Integrated Trajectory (HYSPLIT) model (Stein et al., 2015;  
195 Rolph et al., 2017). Detailed sampling information is listed in Table S1 and includes the  
196 collecting time, location, and the corresponding meteorological data. Black carbon  
197 concentration, air temperature, relative humidity, pressure, relative wind speed, and  
198 wind direction are also shown in Fig. S1.



199  
200 **Figure 1.** Sampling locations with HYSPLIT 72 h backward air mass trajectories. Solid circles  
201 indicate the sample locations. Samples were labeled by numbers. Green, orange, and yellow circles  
202 represent the samples in 35°N – 10°N of Western Pacific (WP-I), 10°N – 40°S of Western Pacific  
203 (WP-II), and 60°S – 80°S of Southern Ocean (SO) regions, respectively. Blue lines show the  
204 backward trajectories starting from 100 m above sea level.



205

## 206 **2.2 Chemical imaging and characterization of particles and INPs**

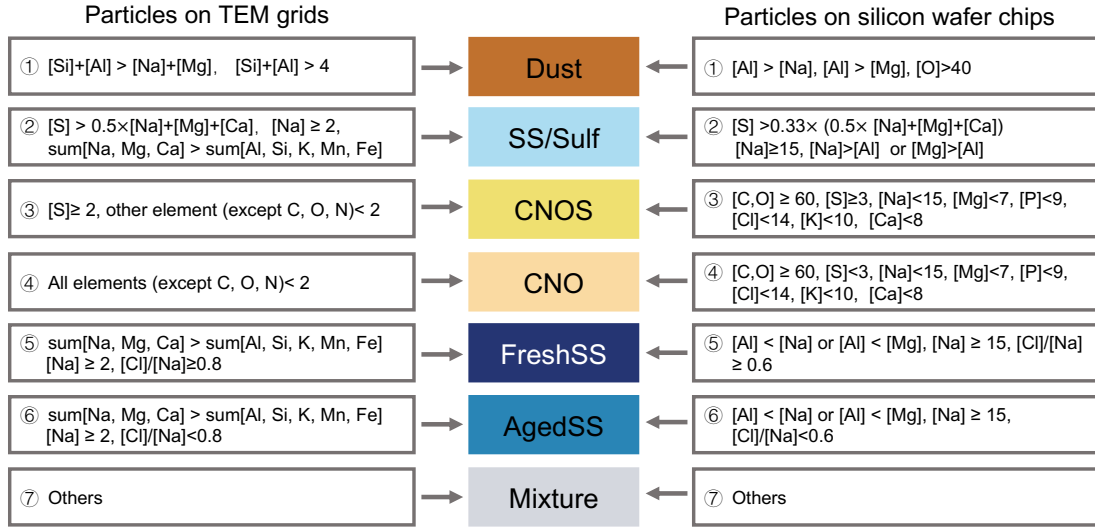
207 Chemical imaging and single particle analysis were used to obtain information on the  
208 morphology, size, and elemental composition of the particle population and INPs. The  
209 methods have been described in detail in previous work (Laskin et al., 2002, 2006, 2012;  
210 Wang et al., 2012a; Knopf et al., 2014; O'Brien et al., 2015) and are briefly introduced  
211 here. Samples collected on the TEM grids were analyzed using a scanning electron  
212 microscope (Quanta 650, FEI Inc.) equipped with an energy dispersive X-ray  
213 spectroscopy (Genesis, EDAX Inc.) in the computer-controlled mode (CCSEM/EDX).  
214 CCSEM/EDX operating at 20 kV first detected the particles and determined their size.  
215 The particle size reported here is the equivalent circle diameter (ECD) based on the  
216 two-dimensional projected area of the particle as determined by CCSEM/EDX analysis.  
217 Particles with a size (ECD) between 0.2  $\mu\text{m}$  and 3  $\mu\text{m}$  were included for analysis in this  
218 study. The elemental composition of each particle was then quantified by determining  
219 the relative atomic percentages of the selected elements, including C, N, O, Na, Mg, Al,  
220 Si, P, S, Cl, K, Ca, Mn, and Fe. We obtained the elemental composition for a significant  
221 number of particles, about 630 – 1480 particles for each sample depending on the  
222 particle loading on the substrates (Table S1). We manually performed SEM/EDX  
223 analysis to characterize the individual identified INPs on the silicon wafer chips after  
224 ice nucleation experiments, as described later. In addition, about 10 particles that did  
225 not nucleate ice (non-INPs) were randomly selected around each INP for SEM/EDX  
226 analysis. X-ray spectra for the INPs and non-INPs were collected at 10 kV. The relative  
227 atomic percentages of elements including C, O, Na, Mg, Al, P, S, Cl, K, and Ca were  
228 quantified. N and Si were not included in the quantification due to their presence in the  
229 background substrate.

230

231 The relative atomic percentage data were analyzed using a rule-based classification  
232 method to assess the contributions of different particle types for each sample (Laskin et  
233 al., 2012; Wang et al., 2012a; China et al., 2018; Lata et al., 2021). As shown in Fig. 2,  
234 the classification scheme grouped particles into seven classes: *i*) “CNO” particles,

235 which mainly contain C, N, and O elements with traces of other elements. These are  
236 carbonaceous particles such as black carbon, secondary or primary organic particles. *ii*)  
237 “CNOS” particles, which mainly contain C, N, O, and S elements with traces of other  
238 elements and are sulfates and other sulfur containing particles including their internal  
239 mixtures with organics. *iii*) “FreshSS” particles, these are fresh sea salt particles  
240 containing Na above a threshold level of 2% (atomic percentage) and with the Cl/Na  
241 ratio > 0.8. At the same time, the total atomic percentage of Na, Mg, and Ca, which are  
242 the dominant cations in sea salt particles, is higher than that of other metals.  
243 CCSEM/EDX analysis of fresh sea salt particles generated by nebulizing sea water  
244 shows that the Cl/Na ratio is slightly higher than 0.8 for particles at about 0.2  $\mu\text{m}$  (Fig.  
245 S2). The samples we investigated contain a large number of small sea salt particles.  
246 Thus, we use a Cl/Na ratio of 0.8 as the threshold value to distinguish between the fresh  
247 and aged sea salt particles. *iv*) “AgedSS” particles, these are aged sea salt particles with  
248 Cl depletion and the Cl/Na ratio < 0.8. *v*) “SS/Sulf” particles, these are aged sea salt  
249 particles mixed with sulfur-containing compounds (e.g., sulfate) containing mainly Na  
250 and S without Cl. *vi*) “Dust” particles, these particles have the total atomic percentage  
251 of Al and Si above 4% and higher than the total atomic percentage of Na and Mg. They  
252 are likely from dust storms and road or soil emissions. *vii*) “Mixture” particles are all  
253 remaining particles that did not fit into the previous categories. The classification  
254 scheme for INPs and non-INPs on silicon wafer chips was modified to account for the  
255 Si and N background in the substrate. It is important to note that particles on either  
256 TEM grids or Si chips were collected at the same time using the same impactor, and  
257 therefore the contributions of the respective particle classes for the two are the same.  
258 Thus, we modified the classification scheme with this assumption.

259



260

261 **Figure 2.** Rule-based particle classification schemes for particles on TEM grids (left) and silicon  
 262 wafer chips (right). Numbers in the schemes are the relative atomic percentages of corresponding  
 263 elements or their ratios.

264

### 265 2.3 Chemical mixing state

266 Chemical mixing state was derived using a previous methodology based on mass and  
 267 entropy metrics (O'Brien et al., 2015; Riemer and West, 2013) and is described briefly  
 268 here. Particle mass was estimated from the density and volume of each particle.  
 269 Particles were assumed to be hemispherical and the volume of each particle was  
 270 calculated from the ECD obtained by CCSEM. Particle density was assigned according  
 271 to its classification, with FreshSS, AgedSS, SS/Sulf, CNO, CNOS, Dust, and Mixture  
 272 particles having a density of 2.0 g/cm<sup>3</sup>, 2.0 g/cm<sup>3</sup>, 1.7 g/cm<sup>3</sup>, 1.3 g/cm<sup>3</sup>, 1.3 g/cm<sup>3</sup>, 2.7  
 273 g/cm<sup>3</sup>, and 2.0 g/cm<sup>3</sup>, respectively (O'Brien et al., 2015; Tang et al., 2014). To calculate  
 274 the mass of each element in a particle, the atomic percentage of each element obtained  
 275 by EDX was converted to a weight percentage, and then multiplied by the mass of the  
 276 particle. For the particle  $i$ , the mass of element  $a$  is equal to:

$$277 \mu_i^a = \mu_i \left( \frac{\text{elemental}\%^a \times \text{molar mass}^a}{\sum_{a=1}^A \text{elemental}\%^a \times \text{molar mass}^a} \right) \quad (1)$$

278 Where  $a = 1, \dots, A$  (number of elements),  $i = 1, \dots, N$  (number of particles), and  $\mu_i$  is  
 279 the total mass of the  $i^{\text{th}}$  particle.  $a$  represents elements of Na, Mg, Al, Si, P, S, Cl, K, Ca,

280 Mn, and Fe, and for this list,  $A = 11$ . Note that C, N, and O are not included as these  
 281 three elements are semi-quantitative when EDX analysis is used (Laskin et al., 2006).

282

283 First, the total mass of element  $a$  in the particle population ( $\mu^a$ ), and the total mass of  
 284 the bulk particle population ( $\mu$ ) were calculated using the following equations,

$$285 \quad \mu^a = \sum_{i=1}^N \mu_i^a, \quad (2)$$

286 and

$$287 \quad \mu = \sum_{i=1}^N \mu_i. \quad (3)$$

288 Then, the mass fraction of element  $a$  in the  $i^{\text{th}}$  particle ( $p_i^a$ ), the mass fraction of  
 289 individual particles ( $p^i$ ) in the particle population, and the mass fraction of element  $a$  in  
 290 the bulk particle population ( $p^a$ ) are

$$291 \quad p_i^a = \frac{\mu_i^a}{\mu_i}, \quad (4)$$

$$292 \quad p_i = \frac{\mu_i}{\mu}, \quad (5)$$

293 and

$$294 \quad p^a = \frac{\mu^a}{\mu}. \quad (6)$$

295 Next, the following Shannon entropies (MacKay, 2003) were calculated, where the  
 296 mixing entropy of the  $i^{\text{th}}$  particle ( $H_i$ ) is

$$297 \quad H_i = \sum_{a=1}^A -p_i^a \ln p_i^a, \quad (7)$$

298 the average particle mixing entropy ( $H_a$ ) is

$$299 \quad H_a = \sum_{i=1}^N p_i H_i, \quad (8)$$

300 and the mass entropy of bulk particle population ( $H_\gamma$ ) is

$$301 \quad H_\gamma = \sum_{a=1}^A -p^a \ln p^a. \quad (9)$$

302  $H_i$  and  $H_\gamma$  are used to describe the mass distribution of species (elements) with the  $i^{\text{th}}$   
 303 particle or particle population, respectively. A higher entropy indicates a more uniform

304 distribution of elements in the individual particle or particle population whereas a lower  
305 entropy towards a non-uniform mass distribution.

306

307 Individual particle diversity ( $D_i$ ) is calculated by taking the exponent of  $H_i$ .  $D_i$  means  
308 the effective number of elements in individual particles, or in other words, indicates the  
309 distribution of elements in single particles.  $D_i$  ranges from the minimum value of 1  
310 when the particle contains a single element to the maximum value of  $A$  when the particle  
311 is composed of all  $A$  elements with equal mass. Particle elemental diversity ( $D_\alpha$ ) and  
312 bulk population elemental diversity ( $D_\gamma$ ) are calculated by taking the exponent of  $H_\alpha$   
313 and  $H_\gamma$ , respectively.  $D_\alpha$  indicates the average effective number of elements in particles.  
314  $D_\gamma$  indicates the effective number of elements in the whole particle sample.

$$315 \quad D_i = e^{H_i} = \prod_{a=1}^A (p_i^a)^{-p_i^a} \quad (10)$$

$$316 \quad D_\alpha = e^{H_\alpha} = \prod_{i=1}^N (D_i)^{p_i} \quad (11)$$

$$317 \quad D_\gamma = e^{H_\gamma} = \prod_{a=1}^A (p^a)^{-p^a} \quad (12)$$

318 The mixing state index ( $\chi$ ) indicates the homogeneity or heterogeneity of the population  
319 and is defined as

$$320 \quad \chi = \frac{D_\alpha - 1}{D_\gamma - 1} \cdot \quad (13)$$

321  $\chi$  ranges from 0% for an externally mixed particle sample with a heterogeneous  
322 population composing single-component particles ( $D_\alpha = 1$ ) to 100% for an internally  
323 well mixed particle sample with a homogeneous population where all particles have  
324 identical compositions.

325

## 326 **2.4 Ice nucleation experiment and INP identification**

327 Ice nucleation and water uptake by particles were examined following our previous  
328 studies (Knopf et al., 2011, 2014, 2022; Wang and Knopf, 2011; Wang et al., 2012b;  
329 Charnawskas et al., 2017; China et al., 2017; Alpert et al., 2022) and the methods are

330 briefly introduced here. Onset conditions of the particle temperature ( $T_p$ ) and relative  
331 humidity with respect to ice ( $RH_{ice}$ ), when ice nucleation and water uptake occurred,  
332 were determined using a custom-built cryo-cooling system. The system consists of a  
333 water vapor control component, an ice nucleation cell (INC), and an optical microscope  
334 (OM). Prior to ice nucleation experiments, a particle sample collected on a silicon wafer  
335 was placed in the INC. Then, a humidified  $N_2$  gas with targeted water vapor partial  
336 pressure was continuously introduced into INC at a flow rate of one standard liter per  
337 minute. The water partial pressure in the INC was determined by the dew point  
338 temperature ( $T_d$ ) of the gas which was measured using a chilled mirror hygrometer (GE  
339 Sensing, Optica). After  $T_d$  was stable,  $T_p$  was set to about  $T_d + 3$  K and  $RH_{ice} < 100\%$ .  
340 An ice nucleation experiment was started and  $T_p$  was cooled at a rate of  $0.2$  K  $min^{-1}$ .  
341 Images of particle sample were recorded by OM every  $0.02$  K.  $T_d$  and  $T_p$  were recorded  
342 every second throughout the experiment. Once ice formation was observed, the sample  
343 was gradually warmed to  $298$  K to sublime and remove any ice that may be retained in  
344 the pores or cavities of particles. Images of ice crystals were acquired during  
345 sublimation at high magnification and the visible particle that served as the INP was  
346 identified after complete crystal sublimation. The experiment was repeated  $3 - 7$  times  
347 at similar  $T_d$  for reproducibility. Water uptake and ice formation by particles were  
348 determined through visual observation and the changes in particle phase or size from  
349 analyzing the recorded images using ImageJ software. through visual observation. DIN  
350 and IMF were discriminated based on whether particles took up water before ice  
351 formation. The freezing mechanism within the small droplets after the water uptake  
352 could not be visualized due to the limited spatial resolution and imaging speed of the  
353 OM used in this study. Thus, we assume that IMF has occurred if the  $RH_{ice}$  onset of  
354 freezing is lower than the homogeneous freezing limits. Only the temperature and  $RH_{ice}$   
355 conditions when the first ice crystal formed were reported.  $RH_{ice}$  was derived from the  
356 measured  $T_d$  and  $T_p$  (Wang and Knopf, 2011). Particle surface area available for ice  
357 nucleation for each sample was estimated from the particle number and size derived  
358 from OM images, assuming that the particles were hemispheres. The conservative  
359 uncertainty of a factor of 2 for particle surface area was estimated using the standard

360 deviation of the means with assumption of particles being flat or spherical. This  
361 assumption likely underestimates the actual surface area since most of the particles  
362 deposited on the substrate exhibited non-spherical geometry and may have had rough  
363 surfaces including cracks or cavities. The particle surface areas were later used for ice  
364 nucleation kinetic analysis. INPs were identified using the recorded optical images  
365 during ice nucleation, ice growth, and ice sublimation. Using these optical images, INPs  
366 were relocated in the SEM using digital pattern recognition and triangulation and then  
367 were imaged and analyzed by SEM/EDX (Knopf et al., 2014).

368

369 The temperature and water vapor distribution within the INC were calibrated and  
370 validated following our previous work (Wang and Knopf, 2011; Wang et al., 2016b).  
371 Homogeneous water vapor distribution in the INC was confirmed by uniform  
372 condensation and evaporation of micro-meter size water droplets across the 0.5 mm<sup>2</sup>  
373 sample area.  $T_p$  was calibrated by the melting points of ice, dodecane, decane, octane,  
374 and heptane. The calibration confirmed that the response of  $T_p$  is linear in the range of  
375 180 – 273 K with an uncertainty less than 0.3 K. Conservative uncertainty in  $RH_{ice}$  for  
376 this experimental system comes from the uncertainty in  $T_d$  and  $T_p$  ( $\Delta T_d < \pm 0.15$  K and  
377  $\Delta T_p < \pm 0.3$  K), resulting in  $\Delta RH_{ice} < \pm 11\%$  at 200 K and  $\Delta RH_{ice} < \pm 3\%$  at 260 K.

378

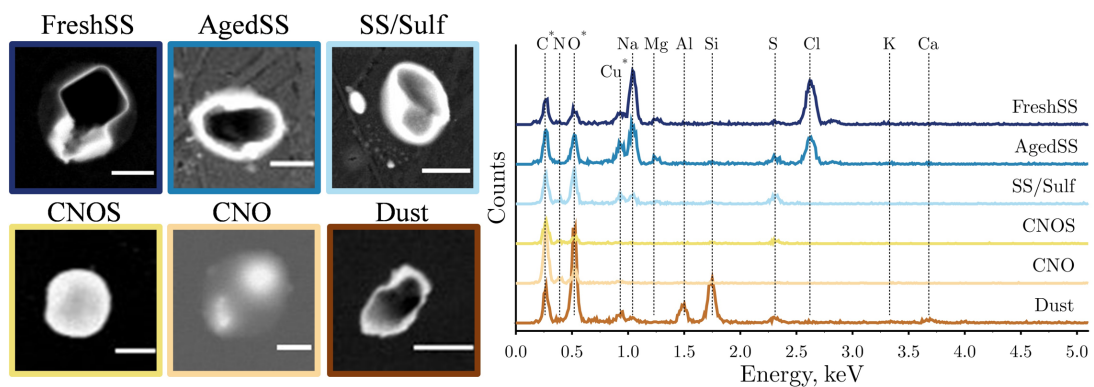
### 379 **3. Results and discussion**

#### 380 **3.1 Particle characterization**

381 Figure 3 shows the typical SEM images and the corresponding EDX spectra of the  
382 identified particle classes. FreshSS and AgedSS particles were dominated by Na with  
383 different contents of Cl. The FreshSS particle exhibited a cubic NaCl crystal  
384 morphology (black solid square) with irregular materials (bright coating) under the  
385 transmission detector of SEM at darkfield mode. The coating likely comprised other  
386 materials in seawater including MgSO<sub>4</sub> and CaSO<sub>4</sub> (Xiao et al., 2008). The AgedSS  
387 particle showed a non-cubic shape NaCl crystal shape as its core is surrounded by  
388 substances containing Na with depletion of Cl. The depletion of Cl indicates that the

389 particle had been aged, possibly due to the formation of gaseous HCl by chemical  
 390 reactions with nitric acid, sulfuric acid, and organic acids in the atmosphere (Laskin et  
 391 al., 2012; Wang et al., 2015; Angle et al., 2021; Su et al., 2022). The SS/Sulf particle  
 392 shown in Fig. 3 had a core-shell structure and was mainly composed of Na and S  
 393 without Cl. This suggests that it was a completely aged sea salt particle coated with  
 394 sulfur-containing components, such as sulfate. The CNOS and CNO particles showed  
 395 a round-shaped morphology. The Dust particle exhibited clear Al and Si peaks with  
 396 minor Ca. Figure 4 shows the particle classification results of over 30,000 particles in  
 397 29 samples investigated by CCSEM/EDX. The size-resolved chemical distributions for  
 398 all samples are shown in Fig. S3, with FreshSS and AgedSS particles dominating all  
 399 size bins. The majority of SS/Sulf particles were larger than 0.5  $\mu\text{m}$ , while the CNOS  
 400 and CNO particles were mainly in the sub-micrometer size range. As shown in Fig. 1  
 401 and Fig. 4, the samples (S1 – S29) were separated into the following three regions  
 402 according to the latitudes of the sampling locations, 35°N – 10°N of the Western Pacific  
 403 (WP-I), 10°N – 40°S of the Western Pacific (WP-II), and 60°S – 80°S of the Southern  
 404 Ocean (SO).

405



406

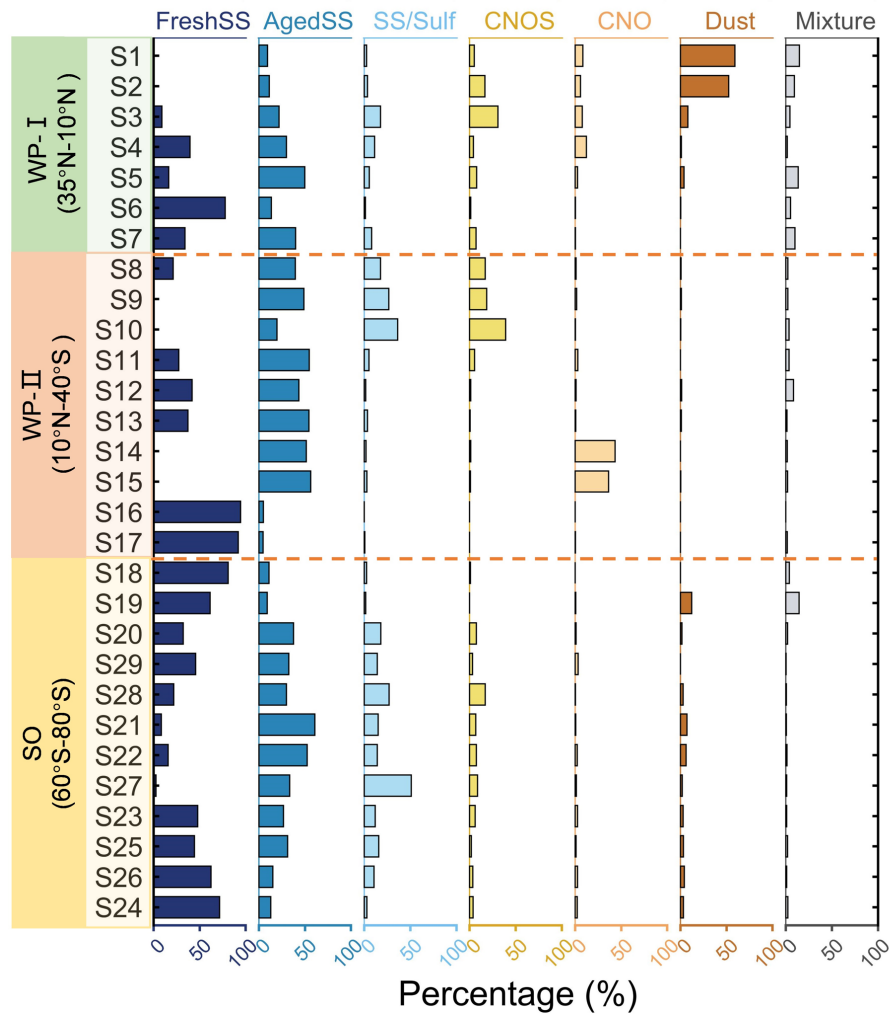
407 **Figure 3.** Representative SEM images and the corresponding EDX spectra for particles from each  
 408 class. The peaks in spectra for the C, O, and Cu elements (asterisked) may include some signal from  
 409 substrate background of TEM grids. SEM images were captured at 20 kV using scanning  
 410 transmission electron microscopy detector. The scale bar for all images is 1  $\mu\text{m}$ .

411

412 Figure 4 shows that in the WP-I region (35°N – 10°N, S1 – S7), the proportion of



413 FreshSS and AgedSS particles increased from 10% to 91% as the ship moved away  
 414 from the land, indicating an increased contribution of SSA. The contribution of the Dust  
 415 particle class decreased from 59% to 8% for S1 to S3. The Navy Aerosol Analysis and  
 416 Prediction System reanalysis (NAAPS-RA) product indicated a dust storm during the  
 417 S1 and S2 sampling periods (Fig. S4). The 72 h backward air mass trajectories also  
 418 showed that the air mass passed through areas affected by the dust storm.



419  
 420 **Figure 4.** Relative percentages of the seven particle classes (FreshSS, AgedSS, SS/Sulf, CNOS,  
 421 CNO, Dust, and Mixture) for each sample sorted by the latitudes of sampling locations and separated  
 422 into three regions (see Fig. 1).

423  
 424 In the WP-II region (10°N – 40°S, S8 – S17), the backward trajectories (Fig. 1) display  
 425 that the air mass of most samples resided over the ocean. However, the samples  
 426 demonstrated large variations in the particle composition. S8 – S10 were dominated by

427 AgedSS, SS/Sulf, and CNOS particles. The percentage of SS/Sulf and CNOS particles  
428 increased from 18% to 36% and from 17% to 39%, respectively, from S8 to S10. The  
429 contributions of these two sulfur-containing particle classes increased simultaneously,  
430 implying the same sulfur source. This is consistent with the results showing high sulfate  
431 aerosol optical depth (AOD) from the NAAPS-RA products at the same period (Fig.  
432 S4D – F). The average BC concentration was  $107.4 \pm 70.6 \text{ ng/m}^3$  for S8 (Table S1). It  
433 likely originated from combustion emissions transported from land. As shown in Fig.  
434 S4C, this is further supported by the air mass for S8 originated around the region where  
435 fire spots were detected in NASA Fire Information for Resource Management System  
436 (FIRMS). S14 and S15 were dominated only by the AgedSS and CNO particles, with  
437 the latter accounting for 43% and 36%, respectively. These higher fractions of CNO  
438 particles compared to other samples (Fig. 4) are likely related to BBA. As shown in Fig.  
439 S1, the average BC concentrations of S14 and S15 were as high as 674 and 356  $\text{ng m}^{-3}$ ,  
440 respectively. Backward trajectories showed that the air mass passed through the high  
441 smoke AOD regions (Fig. S4G – H). These two samples were collected on November  
442 13<sup>th</sup> and 14<sup>th</sup> of 2019, when large wildfires occurred in Australia during the austral  
443 summer of 2019 – 2020 (Hirsch and Koren, 2021). Dense fire spots along the east coast  
444 of Australia at the time of sampling are shown in Fig. S4I. Chemical imaging of  
445 elements (Fig. S5) showed that typical CNO particles from these two samples had thick  
446 organic coatings with high carbon signal inclusions and likely are aged BC. This type  
447 of aged BBA or smoke particles with organic coatings has been observed in the  
448 stratosphere (Ditas et al., 2018). Similar complex organic compounds have also been  
449 observed in the tropospheric smoke aerosol (Palm et al., 2020). Other samples in the  
450 WP-II region (S11, S12, S13, S16, and S17) were dominated by the FreshSS and  
451 AgedSS particles.

452

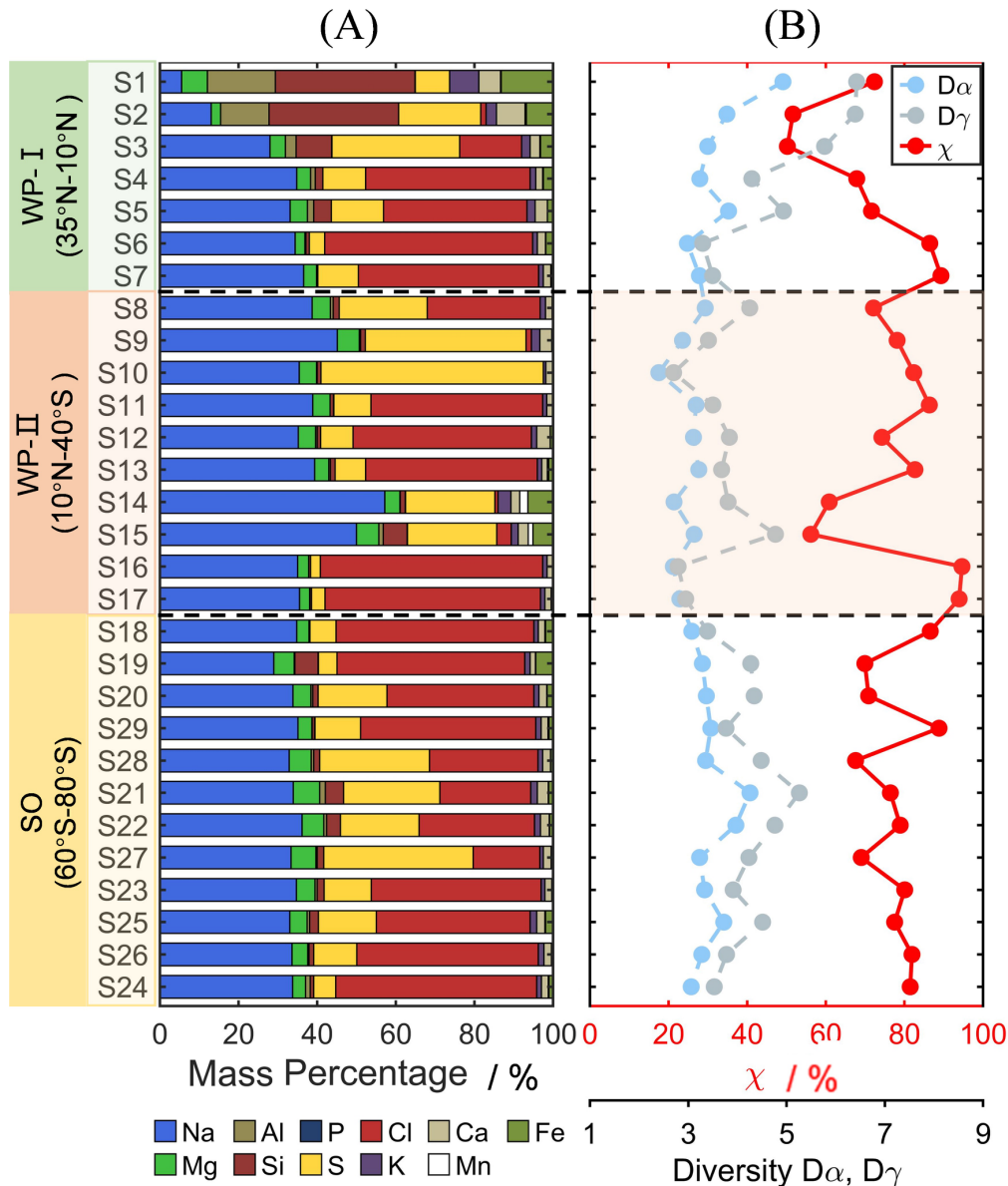
453 In the SO region ( $60^\circ\text{S} - 80^\circ\text{S}$ , sample S18 – S24), the number percentages of FreshSS  
454 particles decreased first and then increased as moving toward higher latitude, whereas  
455 the AgedSS, SS/Sulf, and CNOS particles had opposite trends. These three particle  
456 types contributed to 11% to 93% of the total particles in the sample. As shown in Fig.

457 S6, the contributions of AgedSS, SS/Sulf, and CNOS particles from the middle of the  
458 Ross Sea (S28, S21, S22, S27, S23) were significantly higher than those from the north  
459 (S18, S19, S20, S29) and southwest (S25, S26, S24) of the Ross Sea. The increased  
460 contribution of these three sulfur-containing particle classes may be related to the  
461 biogenic sulfur emission from polynyas (areas of open water surrounded by sea ice) in  
462 the central Ross Sea (Fig. S7) (Brean et al., 2021; Baccharini et al., 2021; McCoy et al.,  
463 2021; Jang et al., 2019; Zhang et al., 2015). The formation of polynyas during the  
464 austral summer allowed phytoplankton to grow and produce DMS which can be  
465 transferred into the atmosphere and oxidized. The products increase the sulfur content  
466 in aerosol particles. Previous work found that the MSA concentration over the Southern  
467 Ocean from November 1994 to February 1995 was about two times higher than that of  
468 the Western Pacific (Kunwar et al., 2023). High MSA levels were observed in the Ross  
469 Sea and were associated with the dynamic sea ice edge at ~64°S in early December  
470 (Yan et al., 2020). This was caused by the increase in phytoplankton from the release  
471 of algae from the melting sea ice. This also suggests the potential impacts by the  
472 biogenic emission of DMS on these samples.

473

474 Except for the two samples impacted by the dust storm, most of the samples collected  
475 during this cruise were predominantly sea salt containing particles including the  
476 FreshSS, AgedSS, and SS/Sulf classes, with total number percentages ranging from 48%  
477 to 99%. The varying proportions of these three particle classes indicated the  
478 contribution of marine emission, but with different degrees of aging which will be  
479 discussed in the next section. Figure S8A and Fig. S9A show the classification results  
480 for super-micron particles (diameter > 1  $\mu\text{m}$ ) and submicron particles (diameter  
481 between 0.2 and 1  $\mu\text{m}$ ), respectively. The sea salt containing particles including  
482 FreshSS, AgedSS, and SS/Sulf classes had higher percentages in the super-micron size  
483 range. The majority of CNOS particles were in the submicron size range. CNOS  
484 represents sulfur containing particles (e.g., sulfate) including their mixtures with  
485 organics. CNOS particles were predominantly in the submicron range, likely due to  
486 new particle formation of MSA and  $\text{H}_2\text{SO}_4$  and their condensation onto pre-existing

487 particles (Hopkins et al., 2008; Yan et al., 2020; Beck et al., 2021). Heterogeneous  
 488 aqueous chemical reactions may also contribute to CNOS particles, including cloud  
 489 processing (e.g., Ervens et al., 2018).



490  
 491 **Figure 5.** Relative mass percentages of elements (A), and mixing state (B) of all samples. Color  
 492 codes for the elements are shown at bottom. Light blue, gray, and red circles represent the particle  
 493 elemental diversity ( $D_\alpha$ ), population elemental diversity ( $D_\gamma$ ), and mixing state index ( $\chi$ ),  
 494 respectively.

495

### 496 3.2 Mixing state of particle population

497 The mixing state described here is based on the elemental composition and is referred

498 to as the chemical mixing state. Figure 5A shows the elemental mass percentages of the  
499 particle population for each sample. Most of the samples were dominated by Na, Cl,  
500 and S, except the samples affected by dust storm (S1, S2). The proportion of Na in each  
501 sample was relatively stable at about 38%. The rest was contributed mostly by Cl and  
502 S. The aging of sea salt particles can be evaluated by the elemental ratio of Cl to Na  
503 (Cl/Na). As shown in Fig. 5A and Fig. S10, the Cl/Na ratio ranges from 0 to close to 1  
504 indicating complete Cl depletion and no aging on sea salt particles, respectively. The  
505 samples with more S have less Cl. This is consistent with the increase in the proportion  
506 of sea salt with different degrees of aging (AgedSS and SS/Sulf). The relationship  
507 between S and Cl indicates that the chlorine loss in particles over ocean is attributed to  
508 the acid displacement by H<sub>2</sub>SO<sub>4</sub> and MSA. The samples affected by the dust storm were  
509 dominated by the elements of Si, Al, and Fe, all of which are common in mineral dust  
510 with traces of Ca and K. As the elements of C, N, and O were not considered in the  
511 mass percentage calculation, the CNO particles prominent in S14 and S15 are not  
512 reflected in the mass percentages (Fig. 5A). The elements of K, Si, and Fe presented in  
513 the same samples are related to biomass burning (Chen et al., 2017). It is consistent  
514 with the air mass from which they were sampled being impacted by biomass burning  
515 plumes.

516

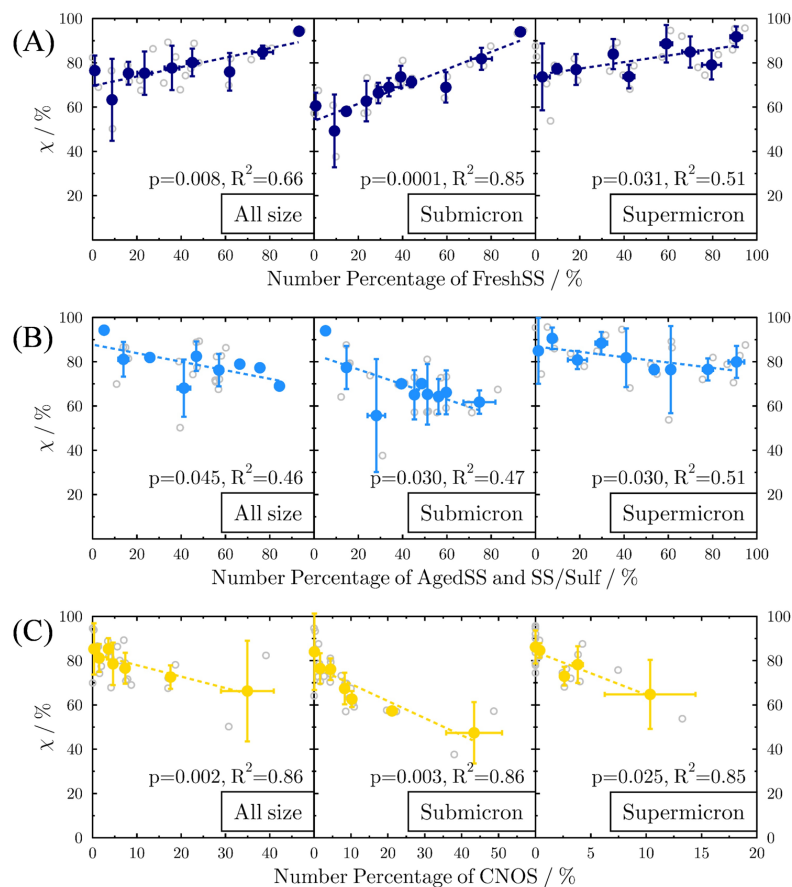
517 The mixing state parameters, namely  $D_\alpha$ ,  $D_\gamma$ , and  $\chi$  for each sample, are presented in  
518 Fig. 5B. The range of  $D_\alpha$  and  $D_\gamma$  was from 2.4 to 4.9 and 2.7 to 6.4, respectively.  $\chi$   
519 ranged from 50% to 95%. In the WP-I region, the Dust-dominated S1 had the highest  
520  $D_\alpha$  of 4.9 and  $D_\gamma$  of 6.4. As the contribution of the Dust particles decreased from 59%  
521 to 1% for S1 to S4,  $D_\alpha$  and  $D_\gamma$  decreased from 4.9 to 3.2 and 6.4 to 4.3, respectively.  $\chi$   
522 first decreased from 72% to 50% (S1 to S3) and then increased to 68% (S4) as the  
523 dominant particle type switched from Dust to sea salt containing particles.  $\chi$  further  
524 increased to 86% (S6) when FreshSS particles dominated. In the WP-II region,  $D_\alpha$  and  
525  $D_\gamma$  decreased as CNOS and SS/Sulf particles increased and the mass percentage of S  
526 increased from S8 to S10, corresponding to a slight increase in  $\chi$  from 72% to 82%.  
527 When comparing the wildfire-influenced samples (S14, S15) and the FreshSS

528 dominated samples (S16, S17), the  $D_\alpha$  values are very similar whereas  $D_\gamma$  values are  
529 quite different (3.8 and 4.8 vs. 2.8 and 2.9) resulting in contrasting  $\chi$  values. The highest  
530  $\chi$  of about 95% for S16 and S17 indicated that these two samples dominated by Na and  
531 Cl were largely internally mixed. This can be expected since they were dominated by  
532 FreshSS particles from the single marine source. AgedSS particles from marine  
533 emission with additional atmospheric processing and CNO particles from biomass  
534 burning had similar contributions to S14 and S15. This was reflected in  $\chi$  of about 58%  
535 for S14 and S15. The main elements of Na and S in these two samples are more  
536 externally mixed. In the SO region,  $D_\alpha$  and  $D_\gamma$  were similar to each other resulting in  
537 relatively stable  $\chi$  values. The changes in  $D_\alpha$  and  $D_\gamma$  are mainly due to the changes in  
538 the contribution of sulfur containing particles. Figure S8 and Fig. S9 show the elemental  
539 mass percentages,  $D_\alpha$ ,  $D_\gamma$ , and  $\chi$  for super-micron and submicron particles, respectively.  
540 For submicron particles of each sample,  $D_\alpha$  and  $D_\gamma$  are 1.9 – 3.9 and 2.4 – 7.1,  
541 respectively.  $\chi$  ranges from about 38% to 95%. For super-micron particles of each  
542 sample,  $D_\alpha$  and  $D_\gamma$  are 2.5 – 5.1 and 2.7 – 6.6, respectively.  $\chi$  ranges from about 54% –  
543 96%. In general,  $D_\alpha$  and  $\chi$  for the submicron particles are lower than super-micron  
544 particles in most samples, whereas  $D_\gamma$  is similar. This suggests that the main elements  
545 of Na, S, and Cl and the minor elements of Mg, K, Fe, Ca, and Si in super-micron  
546 particles tend to be more internally mixed than in submicron particles (Fig. S8B and  
547 Fig. S9B).

548

549 To focus on the effect of particle aging on the mixing state of marine aerosols, we  
550 excluded four samples from two events from the analysis, i.e., the Dust-dominated  
551 samples from a dust storm (S1 and S2) and the BBA-dominated samples from wildfire  
552 emissions (S14 and S15). Figure 6 shows the relationship between  $\chi$  and the percentages  
553 of FreshSS, AgedSS and SS/Sulf, and CNOS particles in different size ranges. To  
554 minimize the potential influence of extreme data points, the linear regression was  
555 performed using the binned data based on the number percentage of particle type. We  
556 found a strong correlation between the percentages of FreshSS particles in the samples  
557 and their  $\chi$  (Fig. 6A,  $R^2 = 0.66$ ,  $p = 0.008$ ), especially for submicron particles ( $R^2 = 0.85$ ).

558  $\chi$  increased as the contribution of FreshSS particles increased. There is a negative  
559 correlation between  $\chi$  and the total percentage of AgedSS and SS/Sulf particles (Fig.  
560 6B,  $R^2 = 0.46$ ,  $p < 0.05$ ). We also found a strong negative correlation between  $\chi$  and the  
561 contribution of CNOS particles (Fig.6C,  $R^2 = 0.86$ ,  $p = 0.002$ ). The results of the above-  
562 mentioned relationship also hold for both submicron and super-micron size range  
563 particles. The positive correlation between the contribution of FreshSS particles and  $\chi$   
564 indicates that the particle population became more internally mixed as more fresh SSA  
565 were added to the air parcel. When the FreshSS particles became the dominant type,  
566 the particle population was close to the complete internal mixing ( $\chi = 100\%$ ), such as  
567 S16 and S17 as discussed above. Adding CNOS particles (a new particle class)  
568 decreases the  $\chi$  and makes the population more externally mixed. These results verify  
569 the schematic descriptions on the evolution of the mixing state described by Riemer et  
570 al (2019) after adding new particles or particles of a dominant type.



571

572 **Figure 6.** Variation of mixing state index ( $\chi$ ) with the number percentages of different particle

573 classes: (A) FreshSS, (B) AgedSS and SS/Sulf, and (C) CNOS. Panels from left to right are for

574 particles with different size ranges: all particle size (All size), 0.2 – 1  $\mu\text{m}$  (Submicron), and larger  
575 than 1  $\mu\text{m}$  in diameter (Super-micron). Original and binned data are shown in open circles and solid  
576 color circles, respectively. Linear regression (dash line) is based on the binned data.

577

578 Atmospheric aging processes can change the composition and mixing state of aerosol  
579 population. In marine environments, the degree of aging on sea salt particles can be  
580 reflected by the contribution of AgedSS and SS/Sulf particles in the population. The  
581 negative correlation between the number percentages of AgedSS and SS/Sulf particles  
582 and  $\chi$  indicates that aging has resulted in a more externally mixed particle population.  
583 This seems to contradict the view that aging tends to drive a particle population towards  
584 a more internally mixed state (Rierner et al., 2019). If an aging process (e.g.,  
585 condensation of secondary organics) occurs uniformly on each particle and further  
586 aging makes them more homogeneous, the population tends to be more internally mixed.  
587 On the other hand, if the aging process occurs only on a specific type of particle, such  
588 as acid displacement turning fresh sea salt into aged sea salt, this will increase particle  
589 diversity and the population may move to a more externally mixed state. This may be  
590 particularly true as fresh sea salt is continuously released even as aged sea salt particles  
591 form. The availability of acids and the size distribution of fresh and aged sea salt  
592 particles at different locations could result in particles with different chlorine  
593 deficiencies and greater diversity. In this case, aging will increase the inhomogeneity  
594 of particles and move the population toward a more externally mixed state.

595

### 596 **3.3 Ice nucleation properties at cirrus conditions**

597 We conducted ice nucleation experiments on six samples dominated by different  
598 particle classes. These samples are separated into four groups: *i*) Dust dominated  
599 sample (S1), where 59% of the particles are dust-like. *ii*) BBA influenced sample (S14)  
600 in which CNO and AgedSS particles contributed 43% and 51%, respectively. *iii*) CNOS  
601 and SS/Sulf dominated sample (S10) with percentages of 39% and 36%, respectively.  
602 *iv*) FreshSS and AgedSS dominated samples (S4, S11, and S12) with a total number  
603 percentage of these two particle types great than 70%. Table 1 shows the dominant



604 particle class, total particle surface area, number of particles available for ice nucleation  
 605 during the experiments, IN-activated fraction at ice nucleation onsets, average ECD of  
 606 INPs and non-INPs, and average ECD of INPs.

607

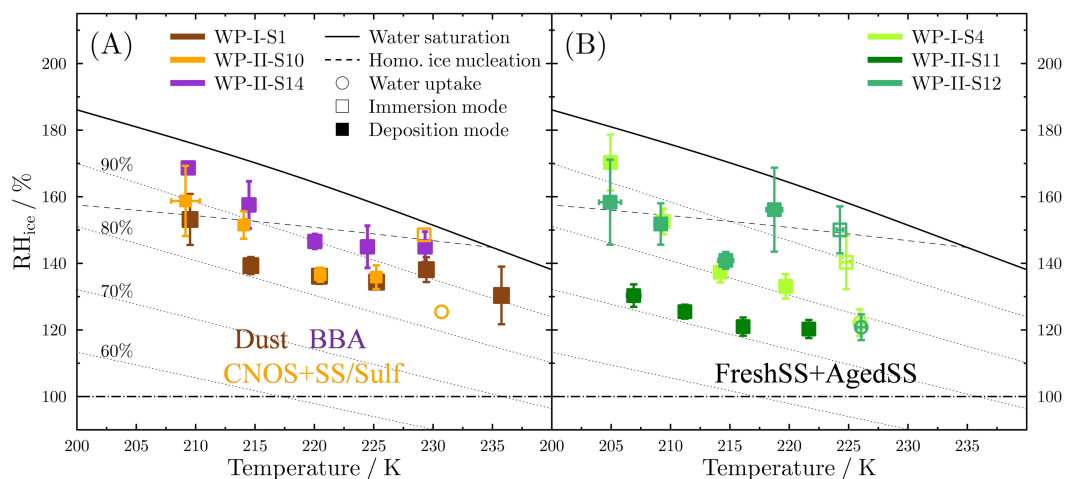
608 **Table 1.** Information of particle samples including the total particle surface area and number of  
 609 particles, IN-activated fraction at ice nucleation onset conditions, the average ECD of INPs and  
 610 non-INPs, and the average ECD of INPs.

Sample	Dominant particle type	Particle surface area ( $\times 10^4 \mu\text{m}^2$ )	Particle number ( $\times 10^5$ )	IN-activated fraction (%)	ECD for INPs ( $\mu\text{m}$ )	ECD for all ( $\mu\text{m}$ )
WP-I-S1	Dust	4.35	0.85	0.12 – 0.24	$2.53 \pm 1.76$	$1.45 \pm 0.98$
WP-I-S4	FreshSS+AgedSS	0.54	1.29	0.08 – 0.15	$0.99 \pm 0.25$	$0.89 \pm 0.25$
WP-II-S10	CNOS+SS/Sulf	6.81	9.13	0.01 – 0.03	$1.54 \pm 0.56$	$1.21 \pm 0.57$
WP-II-S11	FreshSS+AgedSS	7.76	6.37	0.02 – 0.03	$1.19 \pm 0.63$	$1.03 \pm 0.50$
WP-II-S12	FreshSS+AgedSS	12.91	8.26	0.01 – 0.02	$1.91 \pm 1.20$	$1.22 \pm 0.78$
WP-II-S14	BBA	13.84	0.56	0.18	$5.17 \pm 3.12$	$2.50 \pm 2.01$

611

612 Figure 7 shows the onset conditions of  $T_p$  and  $RH_{ice}$  for water uptake and ice nucleation  
 613 on the representative samples. Below 235 K, only DIN was observed for the Dust and  
 614 BBA samples (Fig. 7A). Particles on the Dust sample nucleated ice heterogeneously at  
 615  $RH_{ice}$  from  $130\% \pm 9\%$  to  $153\% \pm 8\%$  at  $T_p$  from 235 K to 209 K. These values are  
 616 below the homogeneous nucleation limits of aqueous droplets (Koop et al., 2000; Koop  
 617 and Zobrist, 2009).  $RH_{ice}$  onsets of the BBA sample ranged from  $145\% \pm 5\%$  to  $169\%$   
 618  $\pm 1\%$  at  $T_p$  from 229 K to 209 K. The  $RH_{ice}$  onsets were only about 3% below the  
 619 homogeneous nucleation limits between 220 K and 228 K, and thus the sample  
 620 dominated by BBA may not have been efficient heterogeneous ice nuclei. As  $T_p$   
 621 decreased, the  $RH_{ice}$  onset of both the BBA and Dust samples gradually increased.  
 622 Particles on the Dust sample initiated DIN at  $RH_{ice}$  lower than the BBA sample by 7%  
 623 to 18% at each  $T_p$ . For the CNOS and SS/Sulf dominated sample (Fig. 7A), particles  
 624 first took up water when  $RH_w$  reached about 83% and then froze via IMF or  
 625 homogeneous nucleation with  $RH_{ice}$  around the homogeneous line at the temperature  
 626 close to 230 K. Particles formed ice via DIN below 225 K at  $RH_{ice}$  from  $136\% \pm 4\%$  to  
 627  $159\% \pm 11\%$ . Figure 7B shows that the ice nucleated on particles from the FreshSS and

628 AgedSS dominated samples via DIN and IMF pathways. The transition temperature  
 629 between DIN and IMF pathways was about 225 K. At about 225 K, particles on S4 and  
 630 S12 both took up water at  $78\% \pm 2\%$  and then formed ice upon further cooling. The  
 631 subsequent ice nucleation of S12 could be homogeneous nucleation or IMF since the  
 632 onset  $RH_{ice}$  of  $150\% \pm 7\%$  is close to the homogeneous nucleation limit. However,  
 633 particles of S4 nucleated ice after water uptake through IMF at  $RH_{ice}$  of  $140\% \pm 8\%$   
 634 which is about 8% lower than the homogeneous nucleation limit. Below 225 K,  
 635 particles of S4 and S12 nucleated ice via DIN at  $RH_{ice}$  from  $133\% \pm 4\%$  to  $170\% \pm 8\%$ .  
 636 DIN occurred on the S11 particles at about  $121\% \pm 3\%$  to  $130\% \pm 3\%$   $RH_{ice}$  below 225  
 637 K. S11 showed the lowest onset  $RH_{ice}$  among the investigated samples indicating that  
 638 its ice nucleation efficiency was higher than other samples. The results of ice nucleation  
 639 onset conditions for the investigated samples showed distinct variations in the ice  
 640 nucleation ability for particles in the different marine atmospheres, even for the samples  
 641 (S11, S12) with similar elemental composition and the dominant particle classes. The  
 642 possible reasons for this are discussed in the later section.



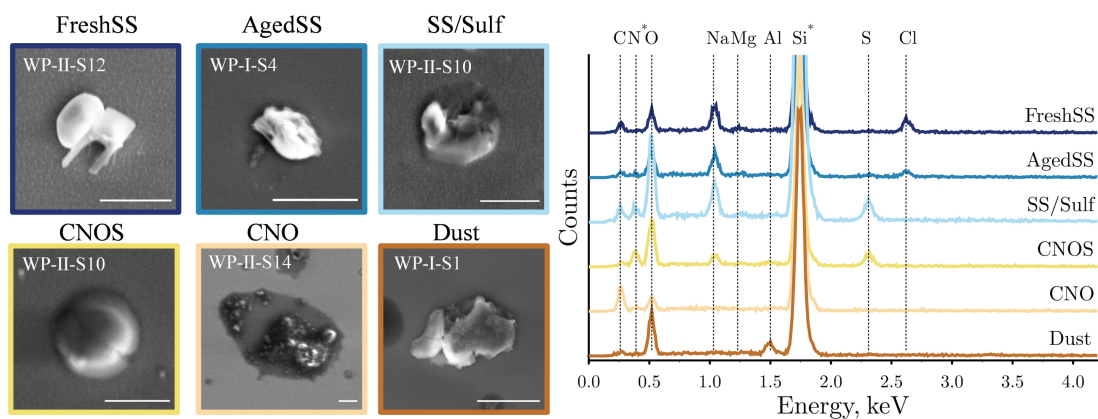
643  
 644 **Figure 7.** Onset conditions of freezing temperature and  $RH_{ice}$  for water uptake (open circles),  
 645 immersion freezing (open squares), and deposition ice nucleation (solid squares) on particle samples.  
 646 (A) Dust dominated sample (S1), BBA influenced sample (S14), and CNOS and SS/Sulf dominated  
 647 sample (S10); (B) FreshSS and AgedSS dominated samples (S4, S11, S12). Dashed line indicates  
 648 the homogeneous freezing limits for aqueous droplets of  $0.3 \mu\text{m}$  in diameter (Koop et al., 2000;  
 649 Koop and Zobrist, 2009). Dotted lines represent different relative humidity ( $RH_w$ ) shown in panel

650 A. Solid and dashed-dotted lines represent water saturation (100%  $RH_w$ ) and ice saturation (100%  
651  $RH_{ice}$ ), respectively.

652

### 653 **3.4 INP characterization**

654 In total, 132 INPs together with 1317 non-INPs on the silicon wafer substrates were  
655 identified and characterized individually for their morphology and elemental  
656 composition. Figure 8 shows the representative SEM images and the corresponding  
657 EDX spectra of different types of INPs. SEM images for each identified INP at different  
658 temperatures are shown in Figs. S11, S12, and S13. The average ECD of INPs was  
659 generally greater than the ECD of the population considering both INPs and non-INPs  
660 together for each sample (Table 1). Of the 132 INPs, 71% of them were super-micron  
661 particles and the rest were submicron particles. The INPs exhibited different  
662 morphologies, such as crystalline irregular shapes (e.g., INPs classified as FreshSS,  
663 Aged SS, and Dust) and spherical shapes (e.g., INPs classified as CNOS). We found  
664 that the majority of INPs from S14 influenced by BBA had thick organic coatings (Fig.  
665 8 and Fig. S11). The organic coating thickness of BBA INPs ( $1.07 \pm 0.68 \mu\text{m}$ ,  $n = 13$ )  
666 is significantly thicker than that of other BBA ( $0.53 \pm 0.37 \mu\text{m}$ ,  $n = 112$ ) at the  
667 significant level of 0.001. Different number fractions of INPs identified in the FreshSS  
668 and AgedSS dominated samples (S4, S11, and S12) have organic coatings. More than  
669 80% of INPs in S11 were coated with organics compared to S4 (33%) and S12 (30%).  
670 Figure S14 shows the elemental mapping of a representative INP with a thin organic  
671 coating. The mapping shows that Na and Cl were distributed in the core, while C and  
672 O were present throughout the whole 2-D projected area of this AgedSS INP. Previous  
673 studies have shown that solid organics can form ice via DIN at low temperatures (Wang  
674 et al., 2012b; Knopf et al., 2018; Lata et al., 2021; Alpert et al., 2022). We speculate  
675 that the organic coatings on the particles of S11 triggered the ice nucleation which have  
676 different ice nucleation abilities compared to S4 and S12.

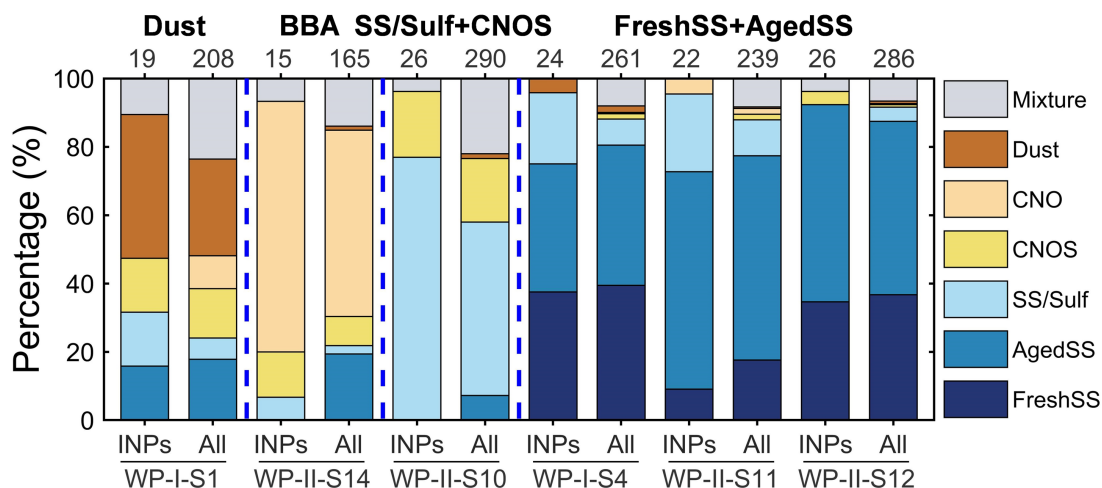


677

678 **Figure 8.** Representative SEM images and the corresponding EDX spectra for 6 classes of INPs.  
 679 The spectra include the substrate background signal of N and Si (asterisk) from silicon wafer  
 680 coated with  $\text{Si}_3\text{N}_4$ . Labels on SEM images are the name of samples. Scale bar is  $2\ \mu\text{m}$  for all images.

681

682 All the identified INPs and non-INPs on the substrates used in the ice nucleation  
 683 experiments were categorized based on the SEM/EDX data. Figure 9 shows the  
 684 percentages of different classes for INPs and the particle population in stacked bars  
 685 marked with “INPs” and “All”, respectively. Taking S1 as an example, six particle  
 686 classes were identified in the particle population and the 19 identified INPs are from  
 687 five particle classes except for the CNO class. Similar to S1, the dominant particle  
 688 classes in the population of all respective samples are also the dominant classes of INPs.  
 689 This result suggests that all these major particle classes identified in our experiments  
 690 are potential INPs. We calculated the average elemental composition of INPs and non-  
 691 INPs for each particle type as shown in Fig. S15. A two-sample t-test was also  
 692 performed on the elemental compositions of INPs and non-INPs for each particle type.  
 693 At the significant level of 0.05, there is no sufficient evidence showing that the  
 694 elemental compositions of INPs and non-INPs are different. We also found that the  
 695 contributions of the same particle class in INPs and the particle population are different  
 696 in some cases. The most notable example is S10 where SS/Sulf particles contributed  
 697 77% of INPs, but only 51% of the population.



698

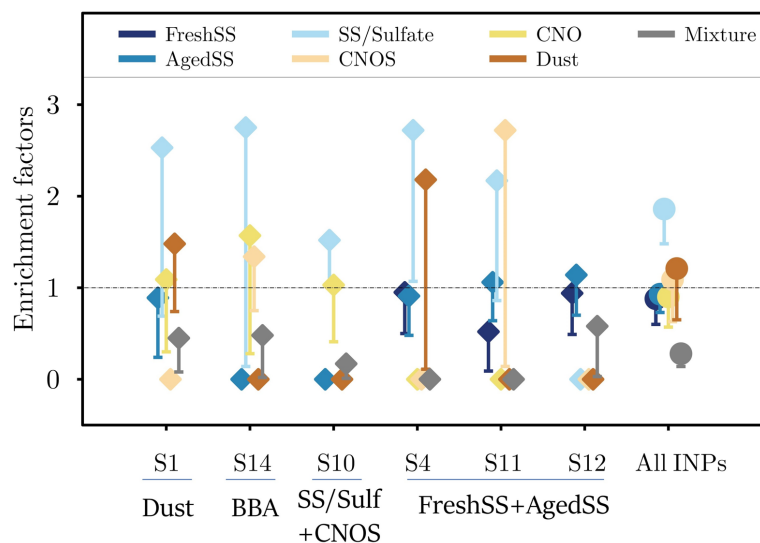
699 **Figure 9.** The number percentages of different particle classes for INPs and the particle population.  
700 Data marked with “All” including both INPs and non-INPs. The corresponding numbers on the top  
701 represent the investigated particle number. Blue dashed lines separate the samples with different  
702 particle classes.

703

704 To further explore whether a particle class is unique when acting as INPs, we calculated  
705 the enrichment factor ( $EF$ ) for a given particle class (A) according to the following  
706 formula:

$$707 \quad EF(A) = \frac{\left( \frac{N_{INPs}^A}{N_{INPs}} \right)}{\left( \frac{N_{INPs+non-INPs}^A}{N_{INPs+non-INPs}} \right)} \quad (14)$$

708 where  $N$  is the number of particles.  $EF(A)$  is the ratio of the contributions of the particle  
709 class A in the INPs to the whole particle population (INPs + non-INPs).  $EF$  values of  
710 each particle class for different samples are shown in Fig. 10.  $EF$  values with upper and  
711 lower limits determined from Poisson distributed errors at 95% confidence level are  
712 listed in Table S2. Although the enriched particle classes are diverse for different  
713 samples,  $EF$  of the SS/Sulf class is greater than 1 for most of the samples except S12.  
714 No INP was identified as SS/Sulf particle for S12 which only has 4% of SS/Sulf in the  
715 population. The overall  $EF$  of the SS/Sulf class is 1.9 with the upper and lower limits  
716 of 9.2 and 1.2, respectively. This indicates that the SS/Sulf particles were enriched in  
717 INPs in these marine environments.



718

719 **Figure 10.** The *EF* of all INP classes for each sample (diamonds) and all INPs (circles). The dashed  
 720 line indicates *EF* of 1. The lower limits of *EF* were calculated by Poisson distribution at the  
 721 confidence level of 95%. For the readability, the upper limits were not plotted here but the values  
 722 are listed in Table S2.

723

### 724 3.5 Comparison of ice nucleation properties with previous studies

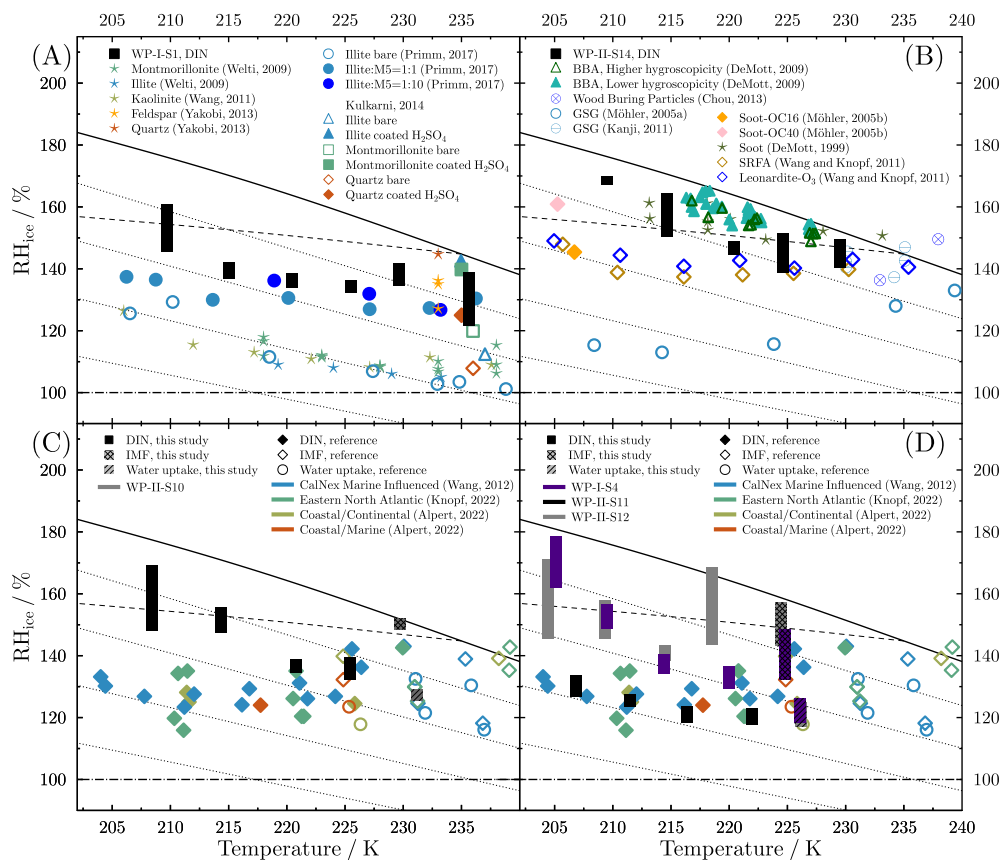
725 Figure 11 shows the comparison of ice nucleation data from our work and previous  
 726 studies. The DIN onset conditions of the Dust dominated sample (S1) are similar to the  
 727 feldspar between 230 K and 235 K (Yakobi-Hancock et al., 2013) and less efficient  
 728 compared to bare dust particles, including montmorillonite (Welti et al., 2009; Kulkarni  
 729 et al., 2014), illite (Welti et al., 2009; Kulkarni et al., 2014), quartz (Kulkarni et al.,  
 730 2014), and kaolinite (Wang and Knopf, 2011). Previous laboratory studies showed that  
 731 the aging processes can reduce the ice nucleation ability of mineral dust at temperatures  
 732 relevant to cirrus clouds (Tang et al., 2016). For example, Primm et al. (2017) indicated  
 733 that the ice nucleation ability of illite can be slightly suppressed by organic acids when  
 734 mixed with a mixture of five dicarboxylic acids (referred to as M5) at an organic-illite  
 735 mass ratio greater than 1:1. The DIN onset conditions of S1 are similar to the M5/illite  
 736 (10:1) mixtures (Fig. 11A). We also found that coated particles (Fig. S16) in S1 serving  
 737 as INPs have a similar coating thickness (Fig. S11) as organic coatings on M5/illite  
 738 greater than 1:1. Kulkarni et al. (2014) observed a decrease in ice nucleation ability of

739 montmorillonite, illite, and quartz at 235 K when coated with H<sub>2</sub>SO<sub>4</sub>. These H<sub>2</sub>SO<sub>4</sub>  
740 coated dust particles had a similar onset  $RH_{ice}$  as compared to particles on S1 at 235 K.  
741 During the cruise, S1 and S2 in the WP-I region were impacted by the dust storm  
742 originating from western Asia. The dust particles were aged during the transport to the  
743 coastal areas and some of them had clear coatings (Fig. S11 and Fig. S16). This is  
744 consistent with the finding by Jang et al.(2023) from the same cruise that aerosol  
745 particles in the S1 sample area have a high fraction of lignin-like organics. S1 had a  
746 similar ice nucleation ability as dust particles with organic coatings. We suspect that the  
747 ice nucleation efficiency of the dust particles at temperatures where DIN occurred on  
748 the INP's surface was affected by coatings after aging.

749

750 Our results for S14 suggest that BBA from the Australian wildfires may have served as  
751 INPs via DIN below 230 K. Combustion and burning processes produce a large number  
752 of particles with mixed organic and inorganic components into the atmosphere (e.g.,  
753 Fuzzi et al., 2007; Chen et al., 2017; Hodshire et al., 2019). Previous studies have shown  
754 that soot, combustion ash, and BBA particles from different burning sources  
755 demonstrated various ice nucleation properties (e.g., Jahl et al., 2021; Jahn et al., 2020;  
756 Kanji et al., 2017 and references therein). Soot particles or their organic coatings on  
757 S14 may have played a role in the observed ice nucleation events. Several studies have  
758 reported that combustion related particles can serve as INPs via DIN below 233 K  
759 (DeMott et al., 1999; Möhler et al., 2005a, b; Koehler et al., 2009; Kanji et al., 2011;  
760 Chou et al., 2013). Kanji et al. (2011) showed the ice nucleation activated by soot  
761 generated using a graphite spark generator (GSG) at about 145%  $RH_{ice}$ , a value similar  
762 to S14 at 230 K. Chou et al. (2013) showed that wood burning particles nucleated ice  
763 at about 136%  $RH_{ice}$  at about 233 K. DeMott et al. (1999) reported that the freezing  
764  $RH_{ice}$  of soot was close to the homogeneous freezing limits. S14 nucleated ice at higher  
765  $RH_{ice}$  than soot generated by GSG and particles containing organic carbon (Möhler et  
766 al., 2005a, b), but lower than the soot studied by DeMott et al. (1999). Suwannee River  
767 standard fulvic acid (SRFA) and leonardite were used as surrogates of atmospheric  
768 organics from biomass burning (Wang and Knopf, 2011). Ice nucleation onset

769 conditions of S14 are very similar to those of SRFA and ozone aged leonardite particles  
 770 above 220 K but higher at lower temperatures.



771  
 772 **Figure 11.** Ice nucleation and water uptake onset conditions (bars) for (A) Dust dominated sample  
 773 (S1), (B) BBA influenced sample (S14), (C) CNOS and SS/Sulf dominated sample (S10), and (D)  
 774 FreshSS and AgedSS dominated samples (S4, S11, S12) compared with previous studies (symbols)  
 775 (DeMott et al., 1999, 2009; Möhler et al., 2005a, b; Welti et al., 2009; Kanji et al., 2011; Wang and  
 776 Knopf, 2011; Wang et al., 2012a; Yakobi-Hancock et al., 2013; Kulkarni et al., 2014; Primm et al.,  
 777 2017; Alpert et al., 2022; Knopf et al., 2022). Descriptions for the lines are the same as in Fig. 7.

778  
 779 Figures 11C and 11D show the comparison of data on marine related particles from  
 780 previous studies with our data on sea salt containing particles. Several studies have  
 781 shown that the aerosol particles collected in marine environments or coastal areas can  
 782 act as efficient INPs at  $RH_{ice}$  between 115% and 143% (e.g., Wang et al., 2012a; Alpert  
 783 et al., 2022; Knopf et al., 2022). Using the micro-spectroscopic analysis, these studies  
 784 identified the INPs and demonstrated that the major particle types in the population



785 initiate ice formation. These particle types include the marine influenced particles with  
786 thin organic coatings collected during the CalNex field campaign (Wang et al., 2012a),  
787 the relatively fresh sea salt particles with marine-produced organics collected from the  
788 coast of Long Island, New York (Alpert et al., 2022), and the processed sea salt  
789 containing particles collected over the eastern North Atlantic (Knopf et al., 2022). There  
790 is one FreshSS and AgedSS dominated sample (S11) that nucleated ice at the same  
791  $RH_{ice}$  onsets as compared to those marine-influenced particles from above mentioned  
792 studies. The other sea salt containing samples in this work including the CNOS and  
793 SS/Sulf dominated sample (S10) and the FreshSS and AgedSS dominated samples (S4,  
794 S12) showed very similar  $RH_{ice}$  onsets only at temperatures above 220 K but higher  
795 onsets below 220 K. The reason for this discrepancy at lower temperatures is not clear.  
796 Future work on the coating composition may provide more insight. Together with  
797 previous studies, we show that these marine influenced particles exhibit different ice  
798 nucleation efficiencies. These variations are likely contributed not only to the complex  
799 compositions but also to the physical and chemical mixing state of these particles.

800

### 801 **3.6 Ice nucleation kinetics**

802 Ice nucleation kinetic analysis was conducted using the experimental data, including  
803 the  $RH_{ice}$  and temperature onsets, particle surface area, number of nucleation events,  
804 and nucleation time. Classical nucleation theory (CNT) has been widely used in cloud  
805 models (e.g., Pruppacher and Klett, 2010; Khvorostyanov and Curry, 2004; Liu and  
806 Penner, 2005). In this study, heterogeneous ice nucleation rate coefficient ( $J_{het}$ ), contact  
807 angle ( $\theta$ ), and their parameterizations are presented and discussed. Ice nucleation  
808 activated fraction of each sample is listed in Table 1 and discussed in Text S2.  $n_s$  based  
809 on the singular hypothesis (Vali, 1971; Connolly et al., 2009) and its parameterizations  
810 are also presented and discussed in Text S2, Fig. S17, and Fig. S18.

811

#### 812 **3.6.1 Heterogeneous ice nucleation rate coefficient ( $J_{het}$ )**

813 According to CNT, ice nucleation is a stochastic process and continues with time, in  
814 contrast to the singular hypothesis (Pruppacher and Klett, 2010).  $J_{het}$  depends on

815 temperature and  $RH_{ice}$ .  $J_{het}$  was derived following the approach in previous works  
816 (Wang and Knopf, 2011; Wang et al., 2012a; China et al., 2017; Knopf et al., 2022).  
817 Using the observed ice nucleation data,  $J_{het} = N_{ice}/(t \times A_{tot})$ , where  $N_{ice}$  is the  
818 number of the observed ice nucleation events that occurred in a temperature interval,  
819  $A_{tot}$  is the total particle surface area available for ice nucleation experiment in the  
820 temperature interval,  $t$  of 6 seconds is the time interval between two consecutive OM  
821 images used to monitor ice formation. In the four groups of particle samples we  
822 investigated,  $J_{het}$  for DIN ranged from 130 to 1370  $\text{cm}^{-2} \text{s}^{-1}$ , 40 to 2970  $\text{cm}^{-2} \text{s}^{-1}$ , 40 to  
823 1480  $\text{cm}^{-2} \text{s}^{-1}$ , and 10 to 390  $\text{cm}^{-2} \text{s}^{-1}$  for the Dust dominated, BBA influenced, CNOS  
824 and SS/Sulf dominated, and FreshSS and AgedSS dominated samples, respectively.  
825  $J_{het}$  for IMF ranged from 540 to 4780  $\text{cm}^{-2} \text{s}^{-1}$  for the FreshSS and AgedSS dominated  
826 samples.

827

### 828 **3.6.2 Parameterizations of $J_{het}$ and $\theta$**

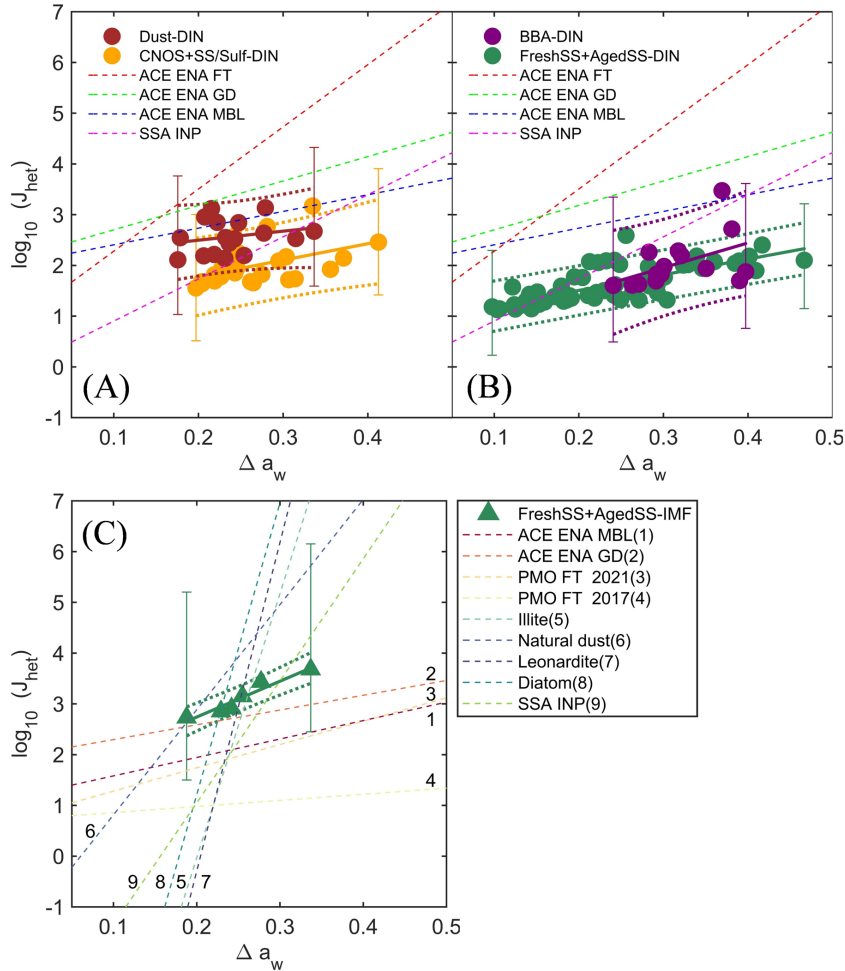
829 The experimentally derived  $J_{het}$  was parameterized based on the water-activity-based  
830 approach. The water-activity-based approach has been widely used to describe the  
831 homogeneous ice nucleation of droplets and depends only on a droplet's water activity  
832 ( $a_w$ ) and  $T_p$  (Koop et al., 2000). Homogeneous ice nucleation temperature follows a  
833 single curve as a function of  $a_w$  and is parameterized by a constant shift of  $a_w$  (i.e.,  
834  $\Delta a_w$ ) from the ice melting temperature curve (Koop and Zobrist, 2009). This approach  
835 has also been applied to heterogeneous ice nucleation including DIN and IMF (Koop  
836 and Zobrist, 2009; Knopf and Alpert, 2013; China et al., 2017). It is assumed that  
837 particles were in equilibrium with the gas phase during the experiments, so  $a_w =$   
838  $RH_w/100$ . For each nucleation event,  $\Delta a_w(T_f)$  is the difference between the  $RH_w$  at  
839 which ice nucleated and the  $RH_w$  on the ice melting curve at the observed ice nucleation  
840 temperature ( $T_f$ ), or  $a_w(T_f)$  and  $a_w^{ice}(T_f)$ , respectively. Then,  $\Delta a_w(T_f) = a_w^{ice}(T_f) -$   
841  $a_w(T_f)$  (Knopf and Alpert, 2013; Koop and Zobrist, 2009), which can be calculated for  
842 each ice nucleation event using the ice nucleation onset temperature and  $RH_w$ .  $J_{het}$  was  
843 calculated for all ice nucleation events and parameterized as a function of  $\Delta a_w$   
844 following the previous works (China et al., 2017; Alpert et al., 2022; Knopf et al., 2022,

845 2023). Figure 12 presents the  $J_{\text{het}}(\Delta a_w)$  for the DIN and IMF data along with the  
846 parameterizations according to  $\log(J_{\text{het}}) = c \times \Delta a_w + d$ . The values of  $c$  and  $d$   
847 parameters are listed in Table 2. The Dust dominated sample has higher  $J_{\text{het}}$  at the same  
848  $\Delta a_w$  compared with the other samples. The BBA influenced sample only nucleated ice  
849 at higher  $\Delta a_w$ . The DIN  $J_{\text{het}}$  for the FreshSS and AgedSS samples changes by 2 orders  
850 of magnitude over a wide range of  $\Delta a_w$ . For the FreshSS and AgedSS samples, IMF  $J_{\text{het}}$   
851 with a larger  $c$  displays a steeper slope than DIN  $J_{\text{het}}$ .

852

853 In Fig. 12, we compared our  $J_{\text{het}}$  parameterizations with previous studies. DIN  $J_{\text{het}}$  of  
854 the Dust-dominated sample is similar to the particles collected during the Aerosol and  
855 Cloud Experiments in the Eastern North Atlantic (ACE ENA) field campaign within  
856 the marine boundary layer (ACE ENA MBL) (Knopf et al., 2022, 2023). It is about 1-  
857 2 orders of magnitude lower than particles collected from the free troposphere (ACE  
858 ENA FT). DIN  $J_{\text{het}}$  of the other particle types investigated in this study are lower than  
859 particles collected from ACE ENA FT, ground site (ACE ENA GD), and ACE ENA  
860 MBL. This is consistent with the results showing that our particles nucleated ice at  
861 higher  $RH_{\text{ice}}$  than particles collected during ACE ENA (Fig. 11). DIN  $J_{\text{het}}$  for the  
862 FreshSS and AgedSS samples is similar to the SSA investigated by Alpert et al. (2022)  
863 in the lower  $\Delta a_w$  range (less than 0.25). This is likely because S11 nucleated ice in this  
864  $\Delta a_w$  range (i.e.,  $RH_{\text{ice}}$ ) is similar to the SSA INP investigated by Alpert et al. (2022) as  
865 they have similar morphology and composition. IMF  $J_{\text{het}}$  of the FreshSS and AgedSS  
866 samples is slightly higher than particles from ACE ENA GD and 1-2 orders of  
867 magnitude higher than the other field samples (Fig. 12C). The IMF  $J_{\text{het}}$  of the FreshSS  
868 and AgedSS samples displays a smaller slope with  $\Delta a_w$  compared to the laboratory-  
869 generated particles, such as illite (Knopf and Alpert, 2013), natural dust (Alpert and  
870 Knopf, 2016; Niemand et al., 2012), leonardite particles (Knopf and Alpert, 2013), and  
871 diatomaceous material (Knopf and Alpert, 2013; Knopf et al., 2011; Alpert et al., 2011a,  
872 b). This is consistent with the study by Knopf et al. (2022) which suggested that the  
873 diversity of ambient particles exhibit different ice nucleation efficiencies compared to  
874 single-component INP types studied in the laboratory at different temperature ranges.

875 Our results emphasize the importance of studying the ice nucleation ability of particles  
 876 and their parameterizations from different geological areas with different diversities in  
 877 particle characteristics.



878  
 879 **Figure 12.**  $J_{\text{het}}$  as a function of  $\Delta a_w$ . Circles represent DIN  $J_{\text{het}}$  for (A) Dust, CNOS and SS/Sulf  
 880 dominated samples, (B) BBA, FreshSS and AgedSS dominated samples. Triangles represent IMF  
 881  $J_{\text{het}}$  (C) for FreshSS and AgedSS dominated samples. Solid lines indicate the fittings according to  
 882  $\log(J_{\text{het}}) = c \times \Delta a_w + d$  with associated dotted lines representing the 95% prediction intervals.  
 883 Representative  $\Delta J_{\text{het}}$  (error bars) are plotted (Text S2). (A-B) Dashed red, green, and blue lines  
 884 represent DIN  $J_{\text{het}}$  parameterizations of particles collected from ACE ENA FT (Knopf et al., 2023),  
 885 ACE ENA GD (Knopf et al., 2022), and ACE ENA MBL (Knopf et al., 2023), respectively. Dashed  
 886 magenta line indicates  $J_{\text{het}}$  for SSA INPs (Alpert et al., 2022). (C) Dashed lines with the number  
 887 label of 1-4 represent IMF  $J_{\text{het}}$  for particles from ACE ENA MBL (Knopf et al., 2023), ACE-ENA  
 888 GD (Knopf et al., 2022), and the Pico Mountain Observatory (PMO) under free-tropospheric (FT)  
 889 conditions in the Azores (PMO FT 2017 and PMO FT 2021) (China et al., 2017; Lata et al., 2021),

890 respectively. Dashed lines with the number label of 5-8 represent IMF  $J_{\text{het}}$  for illite particles (Knopf  
 891 and Alpert, 2013), natural dust (Alpert and Knopf, 2016; Niemand et al., 2012), leonardite particles  
 892 (Knopf and Alpert, 2013), diatomaceous material (Diatom) (Knopf and Alpert, 2013; Knopf et al.,  
 893 2011; Alpert et al., 2011a, b), and SSA INP (Alpert et al., 2022), respectively.

894

895 **Table 2** The  $c$  and  $d$  values for the parameterizations of  $J_{\text{het}}$  as a function of  $\Delta a_w$ ,

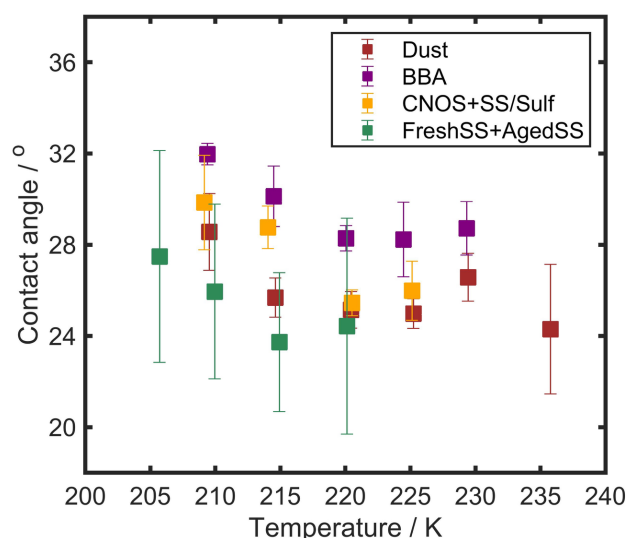
896

$$\log(J_{\text{het}}) = c \times \Delta a_w + d.$$

Sample type	$c$	LCL <sub>c</sub>	UCL <sub>c</sub>	$d$	LCL <sub>d</sub>	UCL <sub>d</sub>	RMSE
Dust-DIN	1.78	-0.15	3.72	2.14	1.67	2.61	0.31
BBA-DIN	4.88	2.38	7.39	0.49	-0.31	1.30	0.43
CNOS+SS/Sulf-DIN	3.24	1.91	4.57	1.13	0.77	1.50	0.35
FreshSS+AgedSS-DIN	3.09	2.76	3.42	0.89	0.81	0.97	0.24
FreshSS+AgedSS-IMF	7.06	6.03	8.09	1.33	1.06	1.60	0.09

897

898  $\theta$  for DIN is derived based on CNT following our previous studies (Wang and Knopf,  
 899 2011; Wang et al., 2012a).  $\theta$  is calculated from  $J_{\text{het}}$  and the ice nucleation onset  
 900 temperature and  $RH_{\text{ice}}$  using the following formula:  $J_{\text{het}} = A \times \exp\left(\frac{-\Delta F_{\text{g,het}}}{kT}\right)$ , where  
 901  $A$  is a pre-exponential factor and  $k$  is the Boltzmann constant.  $\Delta F_{\text{g,het}}$  is the free energy  
 902 of ice embryo formation, which is defined as  $\Delta F_{\text{g,het}} = \frac{16\pi M_w^2 \sigma_{i/v}^3}{3[RT\rho \ln S_{\text{ice}}]^2} \times f(m)$ , where  $R$   
 903 is the universal gas constant,  $\rho$  is the density of ice,  $S_{\text{ice}}$  is the ice saturation ratio ( $S_{\text{ice}} =$   
 904  $RH_{\text{ice}}/100\%$ ),  $M_w$  is the water molecular weight,  $\sigma_{i/v}$  is the surface tension at the ice-  
 905 vapor interface.  $f(m)$  is the geometric factor and is defined as  $f(m) = (m^3 - 3m +$   
 906  $2)/4$ , where  $m = \cos(\theta)$ . A smaller value of  $\theta$  implies higher ice nucleation efficiency  
 907 and should translate to relatively lower  $RH_{\text{ice}}$  onsets in our experiments. Figure 13  
 908 represents the mean  $\theta$  as a function of temperature for INPs of all sample types. When  
 909 comparing  $\theta$  at the same temperature, the FreshSS and AgedSS dominated samples, in  
 910 general, have the smallest  $\theta$ , followed by the Dust dominated, CNOS and SS/Sulf  
 911 dominated, and BBA influenced samples. For all the investigated samples,  $\theta$  was  
 912 relatively constant above 220 K and increased as temperature decreased to 205 K. We  
 913 propose new parameterizations of  $\theta$  as a function of  $T^3 \ln[RH_{\text{ice}}]^2$  (Text S2).  $\theta$  for  
 914 various particle types fall tightly into the parameterization as shown in Fig. S19.



915

916 **Figure 13.** Mean values with one standard deviations of contact angle for DIN by the Dust, BBA,  
 917 CNOS and SS/Sulf, FreshSS and AgedSS dominated samples.

918

### 919 **3.7 Ice nucleation propensity and mixing state of particle population**

920 Previous studies have used  $\chi$  to estimate the error in predicting aerosol CCN activity  
 921 and optical properties when assuming idealized mixing states (Ching et al., 2017; Yao  
 922 et al., 2022). For example, Ching et al. (2017) quantified the error in predicting CCN  
 923 concentration as a function of  $\chi$ . When internal mixing was assumed, errors of up to  
 924 100% overpredicting CCN concentration were found for populations with more  
 925 external mixing ( $\chi < 60\%$ ). However, CCN concentrations were well predicted for  
 926 populations with  $\chi > 75\%$ . Inspired by these studies, we used  $\theta$  as a measure of particle  
 927 ice nucleation propensity to discuss the potential link between the mixed state of  
 928 population and particle ice nucleation propensity. We investigated the relative  
 929 difference (error) in  $\theta$  for the field samples compared to pure NaCl particles. Ice  
 930 nucleation experiments were conducted on the laboratory-generated NaCl particles  
 931 (Text S3) and  $\theta$  was calculated for NaCl particles (see Section 3.6.2 for the calculation  
 932 details). Pure NaCl particles were used as a surrogate of complete internally mixed  
 933 marine aerosols ( $\chi = 100\%$ ). We analyzed the relationship between the relative error in  
 934  $\theta$  of INPs (*Err*) and the mixing state of the population in which the INPs were identified.  
 935 *Err* of each INP from a field sample with a given mixing state ( $\chi$ ) was defined as:

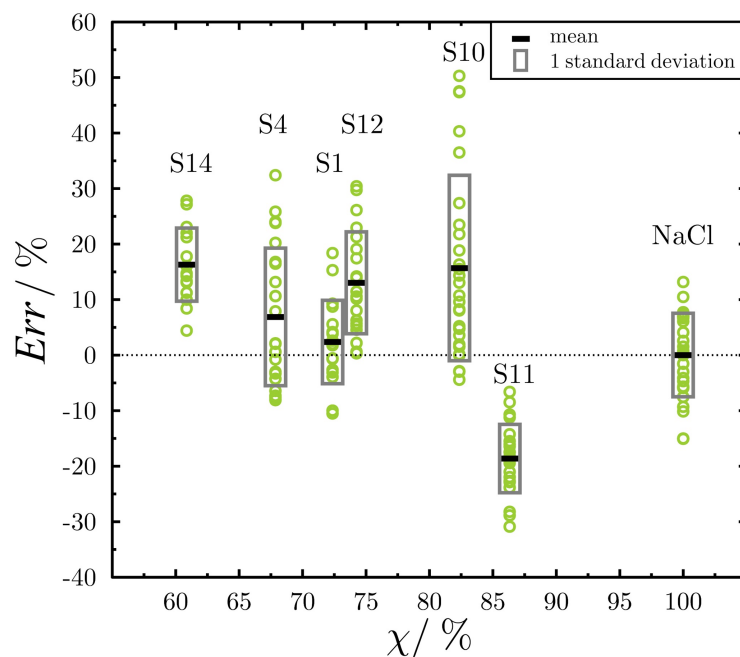
$$936 \quad Err = \frac{\theta(\chi) - \theta(100\%)}{\theta(100\%)} \times 100 \quad (15)$$

937 where  $\theta(100\%)$  is the average  $\theta$  for the NaCl standard. As shown in Fig. 14,  $\chi$  for the  
 938 six investigated samples changed from 61% to 86%. Five samples (S1, S4, S10, S12,  
 939 and S14) exhibited positive mean *Err* ranging from  $2.3\% \pm 7.5\%$  to  $16.3\% \pm 6.6\%$ ,  
 940 while S11 had a negative mean *Err* of  $-18.6\% \pm 6.2\%$ . The FreshSS and AgedSS  
 941 dominated samples, S4 and S12, have a mean *Err* of  $6.9\% \pm 12.4\%$  and  $13.0\% \pm 9.2\%$ ,  
 942 respectively.

943

944 The  $\theta$  for particles in the marine environment is different from that for NaCl particles.  
 945 This can lead to errors in  $J_{\text{het}}$  of several orders of magnitude if the model assumes an  
 946 internally mixed particle population. According to CNT, we calculated DIN  $J_{\text{het}}$  for  
 947 NaCl and particles with *Err* of 5% and 10% under different temperature and humidity  
 948 conditions (Fig. S20). Between 135% and 180%  $RH_{\text{ice}}$ , *Err* of 5% and 10% will result  
 949 in 1.5 – 4 and 2 – 10 orders of magnitude differences in  $J_{\text{het}}$ , respectively. Moreover,  
 950 the lower the temperature and  $RH_{\text{ice}}$ , the larger the error in  $J_{\text{het}}$ . This suggests that the  
 951 effects of aging processes and mixing state need to be considered in the ice nucleation  
 952 modeling for different oceans with complex particle sources, such as coastal regions.  
 953 Instead of pure NaCl, better proxies for SSA should be used in future studies to obtain  
 954 better estimations in *Err* and thus  $J_{\text{het}}$ . No specific correlation or trend was found  
 955 between  $\chi$  and the *Err* from this data set with the limited number of samples. This may  
 956 be expected since ice nucleation is controlled by various physiochemical properties of  
 957 individual particles, particularly for DIN. For example, one crucial factor is the physical  
 958 mixing state of particle, such as coating. Organic coatings play a significant role in  
 959 altering the  $\theta$  of sea salt particles, as exemplified by S11 compared to S4 and S12. In  
 960 contrast to CCN, which in general can be described by the  $\kappa$ -Köhler theory, there are  
 961 still no appropriate physical models to describe INPs. In addition, no direct connection  
 962 between *Err* (i.e.,  $\theta$ ) and  $\chi$  for DIN is likely attributed to the fact that ice nucleation  
 963 propensity for DIN depends on the particle surface composition and morphology on the  
 964 individual particle basis, whereas  $\chi$  characterizes the overall mixing of species (i.e.,

965 composition) within the particle population which may not sensitive to the particle  
 966 surface characteristics. There is a large gap in the understanding of how physical and  
 967 chemical mixing state affects ice nucleation potential of particle population. Other ice  
 968 nucleation variables, e.g., INP concentration, can be used to estimate the potential error  
 969 in cloud modeling if internal mixing is assumed for the population. Mixing state metrics  
 970 reflecting the underlying physical process and the particle physicochemical properties  
 971 controlling ice nucleation ability are needed in future studies, for example, metrics  
 972 measuring the morphological characteristics of particles.



973  
 974 **Figure 14.** *Err* in  $\theta$  for the investigated samples relative to the internally mixed particles (pure  
 975 NaCl particles,  $\chi = 100\%$ ). Black thick lines indicate the average  $\theta$  and the gray boxes represent  
 976 one standard deviation. Green circles represent  $\theta$  for individual INPs.

977

## 978 **4 Atmospheric implications**

979 We found that the distinct mixing states of particle populations were affected by several  
 980 processes over different oceans. In the marine atmosphere that already has a  
 981 contribution of sea salt particles, adding more fresh sea salt particles makes the  
 982 population more internally mixed (Fig. 6). We suspect that over open oceans where sea



983 salt particle flux is large, the population will be mostly internally mixed. The addition  
984 of new particle types from other sources, such as dust storms (WP-I, S1, S2), biomass  
985 burning (WP-II, S14, S15), and secondary sources (CNOS in the SO region), will  
986 decrease the mixing state index and the population will become more externally mixed.  
987 These results are consistent with the proposed schematic description by Riemer et al.  
988 (2019) on the evolution of particle mixing state. We showed that multiphase processes  
989 lead to the aging of fresh sea salt particles resulting in chlorine deficiency and thus  
990 changing the mixing state of the population (Fig. 5). This is a selective process that  
991 occurred on the sea salt particles and is different from the aging by condensation of  
992 secondary materials. As discussed in Section 3.2, these types of selective or  
993 inhomogeneous aging on particles move the population toward a more externally mixed  
994 state. To the best of our knowledge, this is not considered in the models predicting the  
995 mixing state of aerosols, even for the particle-resolved model. Our study suggests that,  
996 when discussing the influence of aging on the evolution of the mixing state, it is  
997 necessary to consider whether the aging processes occur uniformly on all particles.

998

999 We characterized chemical compositions for particle population and INPs at the single  
1000 particle level. We found that all the identified particle types from different sources have  
1001 the potential to serve as INPs, but have different ice nucleation efficiencies (Fig. 7 and  
1002 Fig. 9). We found that S11 showed the highest ice nucleation efficiency among the  
1003 FreshSS and AgedSS dominated samples (Fig. 7), which we attributed to the organic  
1004 coatings on the particles. This indicates the importance of characterizing the physical  
1005 mixing state of particles (i.e., morphology). INPs were enriched in SS/Sulf class,  
1006 suggesting that the aging process alters ice nucleation ability by changing the chemical  
1007 mixing state of particles. Considering the characterizations of individual particles and  
1008 INPs, the ice nucleation onset conditions, and the derived freezing kinetics, it is  
1009 suggested that the ice nucleation abilities at cirrus conditions of these complex marine  
1010 aerosols are affected not only by the particle compositions but also by the mixing state  
1011 of particle population. Future investigations on how the chemical and physical mixing  
1012 state of particles affects ice nucleation in the atmosphere are needed for a better

1013 understanding of aerosol-cloud interactions in the climate system.

1014

1015 According to the CNT, ice nucleation kinetic parameter,  $J_{\text{het}}$ , was derived from the  
1016 experimental data. We proposed parameterizations of  $J_{\text{het}}$  as a function of  $\Delta a_w$  for IMF  
1017 and DIN based on the water-activity based theory. In addition,  $\theta$  was derived for DIN  
1018 based on CNT. We proposed new parameterizations of  $\theta$  taking into account both  
1019 temperature and  $RH_{\text{ice}}$ . These parameterizations can be used to estimate the INP  
1020 concentrations or ice crystal production rates when particle surface area data are  
1021 available. These parameterizations can be used in cloud models with different ice  
1022 nucleation descriptions to evaluate the potential sources and impacts of different  
1023 particles on cloud formation in the marine atmosphere.

1024

## 1025 **5 Conclusions**

1026 Composition, mixing state, and ice nucleation properties were investigated for the  
1027 aerosol particles collected over the Western Pacific and Southern Ocean during a cruise  
1028 from South Korea (34.93°N) to the Ross Sea (75.12°S) in 2019. Seven particle classes  
1029 were identified including fresh sea salt, aged sea salt, sea salt mixed with sulfate,  
1030 carbonaceous particle, sulfur-containing particle, dust, and mixture. Contributions of  
1031 these particles varied across oceans at different latitudes. Except for the samples  
1032 impacted by dust storm, fresh sea salt, aged sea salt, and sea salt mixed with sulfate  
1033 particles were the most prevalent particle types with the total number percentage  
1034 ranging from 48% to 99%. Particles showed different degrees of chloride depletion due  
1035 to the aging processes of acid displacements on sea salt particles. Significant  
1036 contributions of sulfur-containing particles up to 93% in number were found in the Ross  
1037 Sea, which was affected by phytoplankton blooms in the austral summer. The chemical  
1038 mixing state index of particle population ranges from 50% to 95%. The mixing state  
1039 index was positively correlated with the number percentages of fresh sea salt and  
1040 negatively correlated with the proportion of sulfur-containing particles. Particle  
1041 populations tended to be more internally mixed as the fresh sea salt fraction increased.

1042 When sea salt particles were a background or dominant particle type, inhomogeneous  
1043 aging processes and new particle sources made the population more externally mixed.

1044

1045 We showed that different types of particle samples demonstrated a variety of ice  
1046 nucleation abilities at cirrus conditions. The sample dominated by the fresh sea salt  
1047 particles with organic coatings exhibited the highest ice nucleation efficiency with  $RH_{ice}$   
1048 onset as low as 121%, while particles influenced by biomass burning were the least  
1049 efficient among the investigated samples. According to the individual INP  
1050 characterizations, the dominant particle types in the population all contribute to the  
1051 identified INPs but with different enrichment factors. The sea salt mixed with sulfate  
1052 particles were enriched in INPs with an overall factor of about 1.9. Ice nucleation  
1053 abilities of marine aerosol particles were affected not only by composition but also by  
1054 the chemical and physical mixing state of the particle population. Ice nucleation kinetic  
1055 parameters, ice nucleation rate coefficient and contact angle, were derived from the  
1056 experimental data. The corresponding parameterizations for different particle types are  
1057 provided for cloud modeling. In this study, we demonstrated the diversity in the particle  
1058 characteristics at the single particle level, the mixing state of particle population, and  
1059 particles' abilities to form ice crystals in different marine atmospheres in both the  
1060 northern and southern hemispheres. The results motivate the need for further  
1061 investigations of how the mixing state of particles affects ice nucleation in the  
1062 atmosphere.

1063

1064 **Data availability.** All data are given in the main text or in the Supplement. HYSPLIT  
1065 data were obtained through the NOAA website ([https://www.ready.noaa.gov/hypub-  
1066 bin/trajasrc.pl](https://www.ready.noaa.gov/hypub-bin/trajasrc.pl)). NAAPS aerosol reanalysis data were obtained from  
1067 <https://nrlgodae1.nrlmry.navy.mil/ftp/outgoing/nrl/NAAPS-REANALYSIS/>. FIRMS  
1068 data were obtained from <https://firms.modaps.eosdis.nasa.gov/>.

1069

1070 **Supplement.** The supplement related to this article is available online.

1071

1072 **Author contributions.** XJ performed the experiments and wrote the first draft of the  
1073 manuscript. XJ, TZ, JP, and BW performed the data analysis. JP and KP collected  
1074 the samples. BW, JP and KP initiated and designed the study. BW supervised the  
1075 project. BW, YJY, and XJ led the discussion and all authors contributed to the data  
1076 interpretation and the manuscript writing.

1077

1078 **Competing interests.** The authors declare that they have no conflict of interest.

1079

1080 **Acknowledgements.** BW, XJ, and TZ thank the support by National Science  
1081 Foundation of China (42075076, 41775133), Fundamental Research Funds for the  
1082 Central Universities (20720160111, 20720190147). This study is also partially  
1083 funded by the Korea Polar Research Institute research grant (PE23110, PE23030).  
1084 BW and JY thank the support by the Fund of Key Laboratory of Global Change and  
1085 Marine-Atmospheric Chemistry, MNR (GCMAC2004). TZ acknowledges the  
1086 support by the PhD Fellowship of the State Key Laboratory of Marine Environmental  
1087 Science at Xiamen University. We thank the staff onboard R/V *Araon* helping the  
1088 sampling during the Antarctic cruise and Peter A. Alpert for helpful discussion and  
1089 manuscript revision.

1090

## 1091 **References**

1092 Adachi, K., Oshima, N., Gong, Z., de Sá, S., Bateman, A. P., Martin, S. T., de Brito, J. F., Artaxo,  
1093 P., Cirino, G. G., Sedlacek III, A. J., and Buseck, P. R.: Mixing states of Amazon basin aerosol  
1094 particles transported over long distances using transmission electron microscopy, *Atmos.*  
1095 *Chem. Phys.*, 20, 11923–11939, <https://doi.org/10.5194/acp-20-11923-2020>, 2020.

1096 Alpert, P. A. and Knopf, D. A.: Analysis of isothermal and cooling-rate-dependent immersion  
1097 freezing by a unifying stochastic ice nucleation model, *Atmos. Chem. Phys.*, 16, 2083–2107,  
1098 <https://doi.org/10.5194/acp-16-2083-2016>, 2016.

1099 Alpert, P. A., Aller, J. Y., and Knopf, D. A.: Ice nucleation from aqueous NaCl droplets with and  
1100 without marine diatoms, *Atmos. Chem. Phys.*, 11, 5539–5555, <https://doi.org/10.5194/acp-11-5539-2011>, 2011a.

1102 Alpert, P. A., Aller, J. Y., and Knopf, D. A.: Initiation of the ice phase by marine biogenic surfaces  
1103 in supersaturated gas and supercooled aqueous phases, *Phys. Chem. Chem. Phys.*, 13, 19882,  
1104 <https://doi.org/10.1039/c1cp21844a>, 2011b.

1105 Alpert, P. A., Kilhau, W. P., O' Brien, R. E., Moffet, R. C., Gilles, M. K., Wang, B., Laskin, A., Aller,  
1106 J. Y., and Knopf, D. A.: Ice-nucleating agents in sea spray aerosol identified and quantified  
1107 with a holistic multimodal freezing model, *Sci. Adv.*, 8, 1–11,  
1108 <https://doi.org/10.1126/sciadv.abq6842>, 2022.

1109 Angle, K. J., Crocker, D. R., Simpson, R. M. C., Mayer, K. J., Garofalo, L. A., Moore, A. N., Mora  
1110 Garcia, S. L., Or, V. W., Srinivasan, S., Farhan, M., Sauer, J. S., Lee, C., Pothier, M. A., Farmer, D.  
1111 K., Martz, T. R., Bertram, T. H., Cappa, C. D., Prather, K. A., and Grassian, V. H.: Acidity across  
1112 the interface from the ocean surface to sea spray aerosol, *Proc. Natl. Acad. Sci.*, 118, 1–6,  
1113 <https://doi.org/10.1073/pnas.2018397118>, 2021.

1114 Ault, A. P., Moore, M. J., Furutani, H., and Prather, K. A.: Impact of emissions from the Los  
1115 Angeles Port Region on San Diego air quality during regional transport events, *Environ. Sci.  
1116 Technol.*, 43, 3500–3506, <https://doi.org/10/d7kt9s>, 2009.

1117 Ault, A. P., Gaston, C. J., Wang, Y., Dominguez, G., Thiemens, M. H., and Prather, K. A.:  
1118 Characterization of the single particle mixing state of individual ship plume events measured  
1119 at the Port of Los Angeles, *Environ. Sci. Technol.*, 44, 1954–1961,  
1120 <https://doi.org/10.1021/es902985h>, 2010.

1121 Baccharini, A., Dommen, J., Lehtipalo, K., Henning, S., Modini, R. L., Gysel-Beer, M.,  
1122 Baltensperger, U., and Schmale, J.: Low-volatility vapors and new particle formation over the  
1123 Southern Ocean during the Antarctic circumnavigation expedition, *J. Geophys. Res.: Atmos.*,  
1124 126, <https://doi.org/10.1029/2021JD035126>, 2021.

1125 Barnes, I., Hjorth, J., and Mihalopoulos, N.: Dimethyl sulfide and dimethyl sulfoxide and their  
1126 oxidation in the atmosphere, *Chem. Rev.*, 106, 940–975, <https://doi.org/10.1021/cr020529+>,  
1127 2006.

1128 Beck, L. J., Sarnela, N., Junninen, H., Hoppe, C. J. M., Garmash, O., Bianchi, F., Riva, M., Rose,  
1129 C., Peräkylä, O., Wimmer, D., Kausiala, O., Jokinen, T., Ahonen, L., Mikkilä, J., Hakala, J., He, X.,  
1130 Kontkanen, J., Wolf, K. K. E., Cappelletti, D., Mazzola, M., Traversi, R., Petroselli, C., Viola, A. P.,  
1131 Vitale, V., Lange, R., Massling, A., Nøjgaard, J. K., Krejci, R., Karlsson, L., Zieger, P., Jang, S., Lee,  
1132 K., Vakkari, V., Lampilahti, J., Thakur, R. C., Leino, K., Kangasluoma, J., Duplissy, E., Siivola, E.,  
1133 Marbouti, M., Tham, Y. J., Saiz-Lopez, A., Petäjä, T., Ehn, M., Worsnop, D. R., Skov, H., Kulmala,  
1134 M., Kerminen, V., and Sipilä, M.: Differing mechanisms of new particle formation at two Arctic  
1135 sites, *Geophys. Res. Lett.*, 48, 1–11, <https://doi.org/10/gjrb6h>, 2021.

1136 Berndt, T., Hoffmann, E. H., Tilgner, A., Stratmann, F., and Herrmann, H.: Direct sulfuric acid  
1137 formation from the gas-phase oxidation of reduced-sulfur compounds, *Nat. Commun.*, 14,  
1138 4849, <https://doi.org/10/gs3whz>, 2023.

- 1139 Bigg, E. K.: Ice nucleus concentrations in remote areas, *J. Atmos. Sci.*, 30, 1153–1157,  
1140 [https://doi.org/10.1175/1520-0469\(1973\)030\(1153:INCIRA\)2.0.CO;2](https://doi.org/10.1175/1520-0469(1973)030(1153:INCIRA)2.0.CO;2), 1973.
- 1141 Brean, J., Dall’Osto, M., Simó, R., Shi, Z., Beddows, D. C. S., and Harrison, R. M.: Open ocean  
1142 and coastal new particle formation from sulfuric acid and amines around the Antarctic  
1143 Peninsula, *Nat. Geosci.*, 14, 383–388, <https://doi.org/10.1038/s41561-021-00751-y>, 2021.
- 1144 Burrows, S. M., McCluskey, C. S., Cornwell, G., Steinke, I., Zhang, K., Zhao, B., Zawadowicz, M.,  
1145 Raman, A., Kulkarni, G., China, S., Zelenyuk, A., and DeMott, P. J.: Ice-nucleating particles that  
1146 impact clouds and climate: observational and modeling research needs, *Rev. Geophys.*, 60,  
1147 1–45, <https://doi.org/10/gs6w5x>, 2022.
- 1148 Charnawskas, J. C., Alpert, P. A., Lambe, A. T., Berkemeier, T., O’Brien, R. E., Massoli, P.,  
1149 Onasch, T. B., Shiraiwa, M., Moffet, R. C., Gilles, M. K., Davidovits, P., Worsnop, D. R., and Knopf,  
1150 D. A.: Condensed-phase biogenic-anthropogenic interactions with implications for cold cloud  
1151 formation, *Faraday Discuss.*, 200, 165–194, <https://doi.org/10.1039/C7FD00010C>, 2017.
- 1152 Chen, J., Li, C., Ristovski, Z., Milic, A., Gu, Y., Islam, M. S., Wang, S., Hao, J., Zhang, H., He, C.,  
1153 Guo, H., Fu, H., Miljevic, B., Morawska, L., Thai, P., Lam, Y. F., Pereira, G., Ding, A., Huang, X.,  
1154 and Dumka, U. C.: A review of biomass burning: Emissions and impacts on air quality, health  
1155 and climate in China, *Sci. Total Environ.*, 579, 1000–1034,  
1156 <https://doi.org/10.1016/j.scitotenv.2016.11.025>, 2017.
- 1157 Chen, Q., Sherwen, T., Evans, M., and Alexander, B.: DMS oxidation and sulfur aerosol  
1158 formation in the marine troposphere: a focus on reactive halogen and multiphase chemistry,  
1159 *Atmos. Chem. Phys.*, 18, 13617–13637, <https://doi.org/10.5194/acp-18-13617-2018>, 2018.
- 1160 China, S., Alpert, P. A., Zhang, B., Schum, S., Dzepina, K., Wright, K., Owen, R. C., Fialho, P.,  
1161 Mazzoleni, L. R., Mazzoleni, C., and Knopf, D. A.: Ice cloud formation potential by free  
1162 tropospheric particles from long-range transport over the Northern Atlantic Ocean, *J.*  
1163 *Geophys. Res.: Atmos.*, 122, 3065–3079, <https://doi.org/10.1002/2016JD025817>, 2017.
- 1164 China, S., Burrows, S. M., Wang, B., Harder, T. H., Weis, J., Tanarhte, M., Rizzo, L. V., Brito, J.,  
1165 Cirino, G. G., Ma, P.-L., Cliff, J., Artaxo, P., Gilles, M. K., and Laskin, A.: Fungal spores as a source  
1166 of sodium salt particles in the Amazon basin, *Nat. Commun.*, 9, 4793,  
1167 <https://doi.org/10.1038/s41467-018-07066-4>, 2018.
- 1168 Ching, J., Fast, J., West, M., and Riemer, N.: Metrics to quantify the importance of mixing state  
1169 for CCN activity, *Atmos. Chem. Phys.*, 17, 7445–7458, [https://doi.org/10.5194/acp-17-7445-](https://doi.org/10.5194/acp-17-7445-2017)  
1170 2017, 2017.
- 1171 Chou, C., Kanji, Z. A., Stetzer, O., Tritscher, T., Chirico, R., Heringa, M. F., Weingartner, E., Prévôt,  
1172 A. S. H., Baltensperger, U., and Lohmann, U.: Effect of photochemical ageing on the ice  
1173 nucleation properties of diesel and wood burning particles, *Atmos. Chem. Phys.*, 13, 761–772,  
1174 <https://doi.org/10.5194/acp-13-761-2013>, 2013.
- 1175 Cochran, R. E., Ryder, O. S., Grassian, V. H., and Prather, K. A.: Sea spray aerosol: The chemical

1176 link between the oceans, atmosphere, and climate, *Acc. Chem. Res.*, 50, 599–604,  
1177 <https://doi.org/10.1021/acs.accounts.6b00603>, 2017.

1178 Connolly, P. J., Möhler, O., Field, P. R., Saathoff, H., Burgess, R., Choularton, T., and Gallagher,  
1179 M.: Studies of heterogeneous freezing by three different desert dust samples, *Atmos. Chem.*  
1180 *Phys.*, 9, 2805–2824, <https://doi.org/10/bhhzwn>, 2009.

1181 Cornwell, G. C., McCluskey, C. S., Levin, E. J. T., Suski, K. J., DeMott, P. J., Kreidenweis, S. M.,  
1182 and Prather, K. A.: Direct online mass spectrometry measurements of ice nucleating particles  
1183 at a California coastal site, *J. Geophys. Res.: Atmos.*, 124, 12157–12172,  
1184 <https://doi.org/10.1029/2019JD030466>, 2019.

1185 Cziczo, D. J., Ladino, L., Boose, Y., Kanji, Z. A., Kupiszewski, P., Lance, S., Mertes, S., and Wex,  
1186 H.: Measurements of ice nucleating particles and ice residuals, *Meteorol. Monogr.*, 58, 8.1-  
1187 8.13, <https://doi.org/10.1175/AMSMONOGRAPHS-D-16-0008.1>, 2017.

1188 De Leeuw, G., Andreas, E. L., Anguelova, M. D., Fairall, C. W., Lewis, E. R., O' Dowd, C., Schulz,  
1189 M., and Schwartz, S. E.: Production flux of sea spray aerosol, *Rev. Geophys.*, 49, 1–39,  
1190 <https://doi.org/10.1029/2010RG000349>, 2011.

1191 DeMott, P. J., Chen, Y., Kreidenweis, S. M., Rogers, D. C., and Sherman, D. E.: Ice formation by  
1192 black carbon particles, *Geophys. Res. Lett.*, 26, 2429–2432,  
1193 <https://doi.org/10.1029/1999GL900580>, 1999.

1194 DeMott, P. J., Petters, M. D., Prenni, A. J., Carrico, C. M., Kreidenweis, S. M., Collett, J. L., and  
1195 Moosmüller, H.: Ice nucleation behavior of biomass combustion particles at cirrus  
1196 temperatures, *J. Geophys. Res.: Atmos.*, 114, 1–13, <https://doi.org/10.1029/2009JD012036>,  
1197 2009.

1198 DeMott, P. J., Hill, T. C. J., McCluskey, C. S., Prather, K. A., Collins, D. B., Sullivan, R. C., Ruppel,  
1199 M. J., Mason, R. H., Irish, V. E., Lee, T., Hwang, C. Y., Rhee, T. S., Snider, J. R., McMeeking, G. R.,  
1200 Dhaniyala, S., Lewis, E. R., Wentzell, J. J. B., Abbatt, J., Lee, C., Sultana, C. M., Ault, A. P., Axson,  
1201 J. L., Diaz Martinez, M., Venero, I., Santos-Figueroa, G., Stokes, M. D., Deane, G. B., Mayol-  
1202 Bracero, O. L., Grassian, V. H., Bertram, T. H., Bertram, A. K., Moffett, B. F., and Franc, G. D.: Sea  
1203 spray aerosol as a unique source of ice nucleating particles, *Proc. Natl. Acad. Sci.*, 113, 5797–  
1204 5803, <https://doi.org/10.1073/pnas.1514034112>, 2016.

1205 Ditas, J., Ma, N., Zhang, Y., Assmann, D., Neumaier, M., Riede, H., Karu, E., Williams, J., Scharffe,  
1206 D., Wang, Q., Saturno, J., Schwarz, J. P., Katich, J. M., McMeeking, G. R., Zahn, A., Hermann,  
1207 M., Brenninkmeijer, C. A. M., Andreae, M. O., Pöschl, U., Su, H., and Cheng, Y.: Strong impact  
1208 of wildfires on the abundance and aging of black carbon in the lowermost stratosphere, *Proc.*  
1209 *Natl. Acad. Sci.*, 115, E11595–E11603, <https://doi.org/10.1073/pnas.1806868115>, 2018.

1210 Ervens, B., Sorooshian, A., Aldhaif, A. M., Shingler, T., Crosbie, E., Ziemba, L., Campuzano-Jost,  
1211 P., Jimenez, J. L., and Wisthaler, A.: Is there an aerosol signature of chemical cloud processing?,  
1212 *Atmos. Chem. Phys.*, 18, 16099–16119, <https://doi.org/10.5194/acp-18-16099-2018>, 2018.

- 1213 Fraund, M., Pham, D., Bonanno, D., Harder, T., Wang, B., Brito, J., de Sá, S., Carbone, S., China,  
1214 S., Artaxo, P., Martin, S., Pöhlker, C., Andreae, M., Laskin, A., Gilles, M., and Moffet, R.: Elemental  
1215 mixing state of aerosol particles collected in central Amazonia during GoAmazon2014/15,  
1216 *Atmosphere*, 8, 1–27, <https://doi.org/10.3390/atmos8090173>, 2017.
- 1217 Fu, P. Q., Kawamura, K., Chen, J., Charrière, B., and Sempéré, R.: Organic molecular  
1218 composition of marine aerosols over the Arctic Ocean in summer: Contributions of primary  
1219 emission and secondary aerosol formation, *Biogeosciences*, 10, 653–667,  
1220 <https://doi.org/10.5194/bg-10-653-2013>, 2013.
- 1221 Fuzzi, S., Decesari, S., Facchini, M. C., Cavalli, F., Emblico, L., Mircea, M., Andreae, M. O., Trebs,  
1222 I., Hoffer, A., Guyon, P., Artaxo, P., Rizzo, L. V., Lara, L. L., Pauliquevis, T., Maenhaut, W., Raes,  
1223 N., Chi, X., Mayol-Bracero, O. L., Soto-García, L. L., Claeys, M., Kourtchev, I., Rissler, J., Swietlicki,  
1224 E., Tagliavini, E., Schkolnik, G., Falkovich, A. H., Rudich, Y., Fisch, G., and Gatti, L. V.: Overview  
1225 of the inorganic and organic composition of size-segregated aerosol in Rondônia, Brazil, from  
1226 the biomass-burning period to the onset of the wet season, *J. Geophys. Res.: Atmos.*, 112, 1–  
1227 35, <https://doi.org/10.1029/2005JD006741>, 2007.
- 1228 Geng, X., Zhong, G., Li, J., Cheng, Z., Mo, Y., Mao, S., Su, T., Jiang, H., Ni, K., and Zhang, G.:  
1229 Molecular marker study of aerosols in the northern South China Sea: Impact of atmospheric  
1230 outflow from the Indo-China Peninsula and South China, *Atmos. Environ.*, 206, 225–236,  
1231 <https://doi.org/10.1016/j.atmosenv.2019.02.033>, 2019.
- 1232 Gong, X., Wex, H., van Pinxteren, M., Triesch, N., Fomba, K. W., Lubitz, J., Stolle, C., Robinson,  
1233 T.-B., Müller, T., Herrmann, H., and Stratmann, F.: Characterization of aerosol particles at Cabo  
1234 Verde close to sea level and at the cloud level – Part 2: Ice-nucleating particles in air, cloud  
1235 and seawater, *Atmos. Chem. Phys.*, 20, 1451–1468, <https://doi.org/10/ggkghb>, 2020.
- 1236 Han, Y., Fang, X., Xi, X., Song, L., and Yang, S.: Dust storm in Asia continent and its bio-  
1237 environmental effects in the North Pacific: A case study of the strongest dust event in April,  
1238 2001 in central Asia, *Sci. Bull.*, 51, 723–730, <https://doi.org/10.1007/s11434-006-0723-2>,  
1239 2006.
- 1240 Hartmann, M., Adachi, K., Eppers, O., Haas, C., Herber, A., Holzinger, R., Hünerbein, A., Jäkel,  
1241 E., Jentsch, C., Pinxteren, M., Wex, H., Willmes, S., and Stratmann, F.: Wintertime Airborne  
1242 Measurements of Ice Nucleating Particles in the High Arctic: A Hint to a Marine, Biogenic  
1243 Source for Ice Nucleating Particles, *Geophys. Res. Lett.*, 47,  
1244 <https://doi.org/10.1029/2020GL087770>, 2020.
- 1245 Healy, R. M., Sciare, J., Poulain, L., Crippa, M., Wiedensohler, A., Prévôt, A. S. H., Baltensperger,  
1246 U., Sarda-Estève, R., McGuire, M. L., Jeong, C.-H., McGillicuddy, E., O’ Connor, I. P., Sodeau,  
1247 J. R., Evans, G. J., and Wenger, J. C.: Quantitative determination of carbonaceous particle  
1248 mixing state in Paris using single-particle mass spectrometer and aerosol mass spectrometer  
1249 measurements, *Atmos. Chem. Phys.*, 13, 9479–9496, [https://doi.org/10.5194/acp-13-9479-](https://doi.org/10.5194/acp-13-9479-2013)  
1250 2013, 2013.



- 1251 Hirsch, E. and Koren, I.: Record-breaking aerosol levels explained by smoke injection into the  
1252 stratosphere, *Science*, 371, 1269–1274, <https://doi.org/10.1126/science.abe1415>, 2021.
- 1253 Hodshire, A. L., Akherati, A., Alvarado, M. J., Brown-Steiner, B., Jathar, S. H., Jimenez, J. L.,  
1254 Kreidenweis, S. M., Lonsdale, C. R., Onasch, T. B., Ortega, A. M., and Pierce, J. R.: Aging effects  
1255 on biomass burning aerosol mass and composition: a critical review of field and laboratory  
1256 studies, *Environ. Sci. Technol.*, 53, 10007–10022, <https://doi.org/10.1021/acs.est.9b02588>,  
1257 2019.
- 1258 Hoose, C. and Möhler, O.: Heterogeneous ice nucleation on atmospheric aerosols: a review  
1259 of results from laboratory experiments, *Atmos. Chem. Phys.*, 12, 9817–9854,  
1260 <https://doi.org/10.5194/acp-12-9817-2012>, 2012.
- 1261 Hopkins, R. J., Desyaterik, Y., Tivanski, A. V., Zaveri, R. A., Berkowitz, C. M., Tyliczszak, T., Gilles,  
1262 M. K., and Laskin, A.: Chemical speciation of sulfur in marine cloud droplets and particles:  
1263 Analysis of individual particles from the marine boundary layer over the California current, *J.*  
1264 *Geophys. Res.: Atmos.*, 113, 1–15, <https://doi.org/10.1029/2007JD008954>, 2008.
- 1265 Inoue, J., Tobo, Y., Taketani, F., and Sato, K.: Oceanic supply of ice-nucleating particles and its  
1266 effect on ice cloud formation: A case study in the Arctic Ocean during a cold-air outbreak in  
1267 early winter, *Geophys. Res. Lett.*, 48, <https://doi.org/10.1029/2021GL094646>, 2021.
- 1268 IPCC: Climate change 2021: the physical science basis, Cambridge University Press, 2021.
- 1269 Jang, E., Park, K.-T., Yoon, Y. J., Kim, T.-W., Hong, S.-B., Becagli, S., Traversi, R., Kim, J., and  
1270 Gim, Y.: New particle formation events observed at the King Sejong Station, Antarctic  
1271 Peninsula – Part 2: Link with the oceanic biological activities, *Atmos. Chem. Phys.*, 19, 7595–  
1272 7608, <https://doi.org/10.5194/acp-19-7595-2019>, 2019.
- 1273 Jang, J., Park, J., Park, J., Yoon, Y. J., Dall’Osto, M., Park, K.-T., Jang, E., Lee, J. Y., Cho, K. H.,  
1274 and Lee, B. Y.: Ocean-atmosphere interactions: Different organic components across Pacific  
1275 and Southern Oceans, *Sci. Total Environ.*, 878, 1–12, <https://doi.org/10.1016/j.scitotenv.2023.163333>, 2023.
- 1276 Kanji, Z. A., DeMott, P. J., Möhler, O., and Abbatt, J. P. D.: Results from the University of Toronto  
1277 continuous flow diffusion chamber at ICIS 2007: instrument intercomparison and ice onsets  
1278 for different aerosol types, *Atmos. Chem. Phys.*, 11, 31–41, <https://doi.org/10.5194/acp-11-31-2011>,  
1279 2011.
- 1280 Kanji, Z. A., Ladino, L. A., Wex, H., Boose, Y., Burkert-Kohn, M., Cziczo, D. J., and Krämer, M.:  
1281 Overview of ice nucleating particles, *Meteorol. Monogr.*, 58, 1.1–1.33,  
1282 <https://doi.org/10.1175/AMSMONOGRAPHS-D-16-0006.1>, 2017.
- 1283 Khvorostyanov, V. I. and Curry, J. A.: The theory of ice nucleation by heterogeneous freezing  
1284 of deliquescent mixed CCN. Part I: Critical radius, energy, and nucleation rate, *J. Atmos. Sci.*,  
1285 61, 2676–2691, [https://doi.org/10.1175/1520-1730\(2004\)061<2676:TOINBF>2.0.CO;2](https://doi.org/10.1175/1520-1730(2004)061<2676:TOINBF>2.0.CO;2), 2004.
- 1286 Knopf, D. A. and Alpert, P. A.: A water activity based model of heterogeneous ice nucleation

- 1287 kinetics for freezing of water and aqueous solution droplets, *Faraday Discuss.*, 165, 513–534,  
1288 <https://doi.org/10.1039/c3fd00035d>, 2013.
- 1289 Knopf, D. A., Alpert, P. A., Wang, B., and Aller, J. Y.: Stimulation of ice nucleation by marine  
1290 diatoms, *Nat. Geosci.*, 4, 88–90, <https://doi.org/10.1038/ngeo1037>, 2011.
- 1291 Knopf, D. A., Alpert, P. A., Wang, B., O'Brien, R. E., Kelly, S. T., Laskin, A., Gilles, M. K., and  
1292 Moffet, R. C.: Microspectroscopic imaging and characterization of individually identified ice  
1293 nucleating particles from a case field study, *J. Geophys. Res.: Atmos.*, 119, 10,365–10,381,  
1294 <https://doi.org/10.1002/2014JD021866>, 2014.
- 1295 Knopf, D. A., Alpert, P. A., and Wang, B.: The role of organic aerosol in atmospheric ice  
1296 nucleation: a review, *ACS Earth Space Chem.*, 2, 168–202,  
1297 <https://doi.org/10.1021/acsearthspacechem.7b00120>, 2018.
- 1298 Knopf, D. A., Charnawskas, J. C., Wang, P., Wong, B., Tomlin, J. M., Jankowski, K. A., Fraund,  
1299 M., Veghte, D. P., China, S., Laskin, A., Moffet, R. C., Gilles, M. K., Aller, J. Y., Marcus, M. A.,  
1300 Raveh-Rubin, S., and Wang, J.: Micro-spectroscopic and freezing characterization of ice-  
1301 nucleating particles collected in the marine boundary layer in the eastern North Atlantic,  
1302 *Atmos. Chem. Phys.*, 22, 5377–5398, <https://doi.org/10.5194/acp-22-5377-2022>, 2022.
- 1303 Knopf, D. A., Wang, P., Wong, B., Tomlin, J. M., Veghte, D. P., Lata, N. N., China, S., Laskin, A.,  
1304 Moffet, R. C., Aller, J. Y., Marcus, M. A., and Wang, J.: Physicochemical characterization of free  
1305 troposphere and marine boundary layer ice-nucleating particles collected by aircraft in the  
1306 eastern North Atlantic, *Atmos. Chem. Phys.*, 23, 8659–8681, [https://doi.org/10.5194/acp-23-](https://doi.org/10.5194/acp-23-8659-2023)  
1307 [8659-2023](https://doi.org/10.5194/acp-23-8659-2023), 2023.
- 1308 Koehler, K. A., DeMott, P. J., Kreidenweis, S. M., Popovicheva, O. B., Petters, M. D., Carrico, C.  
1309 M., Kireeva, E. D., Khokhlova, T. D., and Shonija, N. K.: Cloud condensation nuclei and ice  
1310 nucleation activity of hydrophobic and hydrophilic soot particles, *Phys. Chem. Chem. Phys.*,  
1311 11, 7906–7920, <https://doi.org/10.1039/b905334b>, 2009.
- 1312 Koop, T. and Zobrist, B.: Parameterizations for ice nucleation in biological and atmospheric  
1313 systems, *Phys. Chem. Chem. Phys.*, 11, 10839, <https://doi.org/10.1039/b914289d>, 2009.
- 1314 Koop, T., Luo, B., Tsias, A., and Peter, T.: Water activity as the determinant for homogeneous  
1315 ice nucleation in aqueous solutions, *Nature*, 406, 611–614, <https://doi.org/10.1038/35020537>,  
1316 2000.
- 1317 Kulkarni, G., Sanders, C., Zhang, K., Liu, X., and Zhao, C.: Ice nucleation of bare and sulfuric  
1318 acid-coated mineral dust particles and implication for cloud properties: Ice formation on dust  
1319 particles, *J. Geophys. Res.: Atmos.*, 119, 9993–10011, <https://doi.org/10.1002/2014JD021567>,  
1320 2014.
- 1321 Kunwar, B., Pokhrel, A., Niwai, T., and Kawamura, K.: Spatial and longitudinal distributions of  
1322 total carbon, nitrogen and sulfur together with water-soluble major ions in marine aerosols  
1323 collected from the Western Pacific and Southern Ocean, *J. Geophys. Res.: Atmos.*, 128, 1–23,

- 1324 <https://doi.org/10.1029/2022JD037874>, 2023.
- 1325 Ladino, L. A., Yakobi-Hancock, J. D., Kilthau, W. P., Mason, R. H., Si, M., Li, J., Miller, L. A.,  
1326 Schiller, C. L., Huffman, J. A., Aller, J. Y., Knopf, D. A., Bertram, A. K., and Abbatt, J. P. D.:  
1327 Addressing the ice nucleating abilities of marine aerosol: A combination of deposition mode  
1328 laboratory and field measurements, *Atmos. Environ.*, 132, 1–10,  
1329 <https://doi.org/10.1016/j.atmosenv.2016.02.028>, 2016.
- 1330 Ladino, L. A., Raga, G. B., Alvarez-Ospina, H., Andino-Enríquez, M. A., Rosas, I., Martínez, L.,  
1331 Salinas, E., Miranda, J., Ramírez-Díaz, Z., Figueroa, B., Chou, C., Bertram, A. K., Quintana, E. T.,  
1332 Maldonado, L. A., García-Reynoso, A., Si, M., and Irish, V. E.: Ice-nucleating particles in a  
1333 coastal tropical site, *Atmos. Chem. Phys.*, 19, 6147–6165, <https://doi.org/10/gpjrd4>, 2019.
- 1334 Laskin, A., Iedema, M. J., and Cowin, J. P.: Quantitative time-resolved monitoring of nitrate  
1335 formation in sea salt particles using a CCSEM/EDX single particle analysis, *Environ. Sci.*  
1336 *Technol.*, 36, 4948–4955, <https://doi.org/10.1021/es020551k>, 2002.
- 1337 Laskin, A., Cowin, J. P., and Iedema, M. J.: Analysis of individual environmental particles using  
1338 modern methods of electron microscopy and X-ray microanalysis, *J. Electron. Spectrosc. Relat.*  
1339 *Phenom.*, 150, 260–274, <https://doi.org/10.1016/j.elspec.2005.06.008>, 2006.
- 1340 Laskin, A., Moffet, R. C., Gilles, M. K., Fast, J. D., Zaveri, R. A., Wang, B., Nigge, P., and  
1341 Shutthanandan, J.: Tropospheric chemistry of internally mixed sea salt and organic particles:  
1342 Surprising reactivity of NaCl with weak organic acids, *J. Geophys. Res.: Atmos.*, 117, 1–12,  
1343 <https://doi.org/10.1029/2012JD017743>, 2012.
- 1344 Lata, N. N., Zhang, B., Schum, S., Mazzoleni, L., Brimberry, R., Marcus, M. A., Cantrell, W. H.,  
1345 Fialho, P., Mazzoleni, C., and China, S.: Aerosol composition, mixing state, and phase state of  
1346 free tropospheric particles and their role in ice cloud formation, *ACS Earth Space Chem.*, 5,  
1347 3499–3510, <https://doi.org/10.1021/acsearthspacechem.1c00315>, 2021.
- 1348 Li, W., Shao, L., Zhang, D., Ro, C.-U., Hu, M., Bi, X., Geng, H., Matsuki, A., Niu, H., and Chen, J.:  
1349 A review of single aerosol particle studies in the atmosphere of East Asia: morphology, mixing  
1350 state, source, and heterogeneous reactions, *J. Clean. Prod.*, 112, 1330–1349,  
1351 <https://doi.org/10.1016/j.jclepro.2015.04.050>, 2016.
- 1352 Liu, X. and Penner, J. E.: Ice nucleation parameterization for global models, *Meteor. Z.*, 499–  
1353 514, <https://doi.org/10/b3b83s>, 2005.
- 1354 Liu, Y., Minofar, B., Desyaterik, Y., Dames, E., Zhu, Z., Cain, J. P., Hopkins, R. J., Gilles, M. K.,  
1355 Wang, H., Jungwirth, P., and Laskin, A.: Internal structure, hygroscopic and reactive properties  
1356 of mixed sodium methanesulfonate-sodium chloride particles, *Phys. Chem. Chem. Phys.*, 13,  
1357 11846–11857, <https://doi.org/10.1039/c1cp20444k>, 2011.
- 1358 MacKay, D. J. C.: Information theory, inference, and learning algorithms, Cambridge University  
1359 Press, Cambridge, 628 pp., 2003.

- 1360 Mason, R. H., Si, M., Li, J., Chou, C., Dickie, R., Toom-Sauntry, D., Pöhlker, C., Yakobi-Hancock,  
1361 J. D., Ladino, L. A., Jones, K., Leaitch, W. R., Schiller, C. L., Abbatt, J. P. D., Huffman, J. A., and  
1362 Bertram, A. K.: Ice nucleating particles at a coastal marine boundary layer site: correlations  
1363 with aerosol type and meteorological conditions, *Atmos. Chem. Phys.*, 15, 12547–12566,  
1364 <https://doi.org/10.5194/acp-15-12547-2015>, 2015.
- 1365 McCluskey, C. S., Hill, T. C. J., Malfatti, F., Sultana, C. M., Lee, C., Santander, M. V., Beall, C. M.,  
1366 Moore, K. A., Cornwell, G. C., Collins, D. B., Prather, K. A., Jayarathne, T., Stone, E. A., Azam, F.,  
1367 Kreidenweis, S. M., and DeMott, P. J.: A dynamic link between ice nucleating particles released  
1368 in nascent sea spray aerosol and oceanic biological activity during two mesocosm  
1369 experiments, *J. Atmos. Sci.*, 74, 151–166, <https://doi.org/10.1175/JAS-D-16-0087.1>, 2017.
- 1370 McCluskey, C. S., Ovadnevaite, J., Rinaldi, M., Atkinson, J., Belosi, F., Ceburnis, D., Marullo, S.,  
1371 Hill, T. C. J., Lohmann, U., Kanji, Z. A., O' Dowd, C., Kreidenweis, S. M., and DeMott, P. J.:  
1372 Marine and terrestrial organic ice-nucleating particles in pristine marine to continentally  
1373 influenced Northeast Atlantic air masses, *J. Geophys. Res.: Atmos.*, 123, 6196–6212,  
1374 <https://doi.org/10/gpjrjh>, 2018a.
- 1375 McCluskey, C. S., Hill, T. C. J., Humphries, R. S., Rauker, A. M., Moreau, S., Stratton, P. G.,  
1376 Chambers, S. D., Williams, A. G., McRobert, I., Ward, J., Keywood, M. D., Harnwell, J., Ponsonby,  
1377 W., Loh, Z. M., Krummel, P. B., Protat, A., Kreidenweis, S. M., and DeMott, P. J.: Observations  
1378 of ice nucleating particles over Southern Ocean waters, *Geophys. Res. Lett.*, 45, 11–989,  
1379 <https://doi.org/10.1029/2018GL079981>, 2018b.
- 1380 McCoy, I. L., Bretherton, C. S., Wood, R., Twohy, C. H., Gettelman, A., Bardeen, C. G., and  
1381 Toohey, D. W.: Influences of recent particle formation on Southern Ocean aerosol variability  
1382 and low cloud properties, *Journal of Geophysical Research: Atmospheres*, 126,  
1383 e2020JD033529, <https://doi.org/10.1029/2020JD033529>, 2021.
- 1384 Möhler, O., Büttner, S., Linke, C., Schnaiter, M., Saathoff, H., Stetzer, O., Wagner, R., Krämer,  
1385 M., Mangold, A., Ebert, V., and Schurath, U.: Effect of sulfuric acid coating on heterogeneous  
1386 ice nucleation by soot aerosol particles, *J. Geophys. Res.: Atmos.*, 110, 1–12,  
1387 <https://doi.org/10.1029/2004JD005169>, 2005a.
- 1388 Möhler, O., Linke, C., Saathoff, H., Schnaiter, M., Wagner, R., Mangold, A., Krämer, M., and  
1389 Schurath, U.: Ice nucleation on flame soot aerosol of different organic carbon content, *Meteor.*  
1390 *Z.*, 14, 477–484, <https://doi.org/10.1127/0941-2948/2005/0055>, 2005b.
- 1391 Murray, B. J., O'Sullivan, D., Atkinson, J. D., and Webb, M. E.: Ice nucleation by particles  
1392 immersed in supercooled cloud droplets, *Chem. Soc. Rev.*, 41, 6519–6554,  
1393 <https://doi.org/10.1039/c2cs35200a>, 2012.
- 1394 Myriokefalitakis, S., Vignati, E., Tsigaridis, K., Papadimas, C., Sciare, J., Mihalopoulos, N.,  
1395 Facchini, M. C., Rinaldi, M., Dentener, F. J., Ceburnis, D., Hatzianastasiou, N., O' Dowd, C. D.,  
1396 van Weele, M., and Kanakidou, M.: Global modeling of the oceanic source of organic aerosols,  
1397 *Adv. Meteorol.*, 2010, 1–16, <https://doi.org/10.1155/2010/939171>, 2010.

- 1398 Niemand, M., Möhler, O., Vogel, B., Vogel, H., Hoose, C., Connolly, P., Klein, H., Bingemer, H.,  
1399 DeMott, P., Skrotzki, J., and Leisner, T.: A particle-surface-area-based parameterization of  
1400 immersion freezing on desert dust particles, *J. Atmos. Sci.*, 69, 3077–3092,  
1401 <https://doi.org/10/f4bkk>, 2012.
- 1402 O'Brien, R. E., Wang, B., Laskin, A., Riemer, N., West, M., Zhang, Q., Sun, Y., Yu, X., Alpert, P.,  
1403 Knopf, D. A., Gilles, M. K., and Moffet, R. C.: Chemical imaging of ambient aerosol particles:  
1404 Observational constraints on mixing state parameterization, *J. Geophys. Res.: Atmos.*, 120,  
1405 9591–9605, <https://doi.org/10.1002/2015JD023480>, 2015.
- 1406 Palm, B. B., Peng, Q., Fredrickson, C. D., Lee, B. H., Garofalo, L. A., Pothier, M. A., Kreidenweis,  
1407 S. M., Farmer, D. K., Pokhrel, R. P., Shen, Y., Murphy, S. M., Permar, W., Hu, L., Campos, T. L.,  
1408 Hall, S. R., Ullmann, K., Zhang, X., Flocke, F., Fischer, E. V., and Thornton, J. A.: Quantification  
1409 of organic aerosol and brown carbon evolution in fresh wildfire plumes, *Proc. Natl. Acad. Sci.*  
1410 *U.S.A.*, 117, 29469–29477, <https://doi.org/10.1073/pnas.2012218117>, 2020.
- 1411 Park, J., Dall'Osto, M., Park, K., Gim, Y., Kang, H. J., Jang, E., Park, K.-T., Park, M., Yum, S. S.,  
1412 Jung, J., Lee, B. Y., and Yoon, Y. J.: Shipborne observations reveal contrasting Arctic marine,  
1413 Arctic terrestrial and Pacific marine aerosol properties, *Atmos. Chem. Phys.*, 20, 5573–5590,  
1414 <https://doi.org/10.5194/acp-20-5573-2020>, 2020.
- 1415 Park, J. Y., Lim, S., and Park, K.: Mixing state of submicrometer sea spray particles enriched by  
1416 insoluble species in bubble-bursting experiments, *J. Atmos. Ocean. Technol.*, 31, 93–104,  
1417 <https://doi.org/10.1175/JTECH-D-13-00086.1>, 2014.
- 1418 Prather, K. A., Bertram, T. H., Grassian, V. H., Deane, G. B., Stokes, M. D., DeMott, P. J., Aluwihare,  
1419 L. I., Palenik, B. P., Azam, F., Seinfeld, J. H., Moffet, R. C., Molina, M. J., Cappa, C. D., Geiger, F.  
1420 M., Roberts, G. C., Russell, L. M., Ault, A. P., Baltrusaitis, J., Collins, D. B., Corrigan, C. E., Cuadra-  
1421 Rodriguez, L. A., Ebben, C. J., Forestieri, S. D., Guasco, T. L., Hersey, S. P., Kim, M. J., Lambert,  
1422 W. F., Modini, R. L., Mui, W., Pedler, B. E., Ruppel, M. J., Ryder, O. S., Schoepp, N. G., Sullivan,  
1423 R. C., and Zhao, D.: Bringing the ocean into the laboratory to probe the chemical complexity  
1424 of sea spray aerosol, *Proc. Natl. Acad. Sci.*, 110, 7550–7555,  
1425 <https://doi.org/10.1073/pnas.1300262110>, 2013.
- 1426 Primm, K. M., Schill, G. P., Veghte, D. P., Freedman, M. A., and Tolbert, M. A.: Depositional ice  
1427 nucleation on NX illite and mixtures of NX illite with organic acids, *J. Atmos. Chem.*, 74, 55–  
1428 69, <https://doi.org/10.1007/s10874-016-9340-x>, 2017.
- 1429 Pruppacher, H. R. and Klett, J. D.: *Microphysics of clouds and precipitation*, Springer  
1430 Netherlands, Dordrecht, 954 pp., <https://doi.org/10.1007/978-0-306-48100-0>, 2010.
- 1431 Riemer, N. and West, M.: Quantifying aerosol mixing state with entropy and diversity  
1432 measures, *Atmos. Chem. Phys.*, 13, 11423–11439, [https://doi.org/10.5194/acp-13-11423-](https://doi.org/10.5194/acp-13-11423-2013)  
1433 2013, 2013.
- 1434 Riemer, N., Ault, A. P., West, M., Craig, R. L., and Curtis, J. H.: Aerosol mixing state:

1435 measurements, modeling, and impacts, *Rev. Geophys.*, 57, 187–249,  
1436 <https://doi.org/10.1029/2018RG000615>, 2019.

1437 Rolph, G., Stein, A., and Stunder, B.: Real-time environmental applications and display system:  
1438 ready, *Environ. Model Softw.*, 95, 210–228, <https://doi.org/10.1016/j.envsoft.2017.06.025>,  
1439 2017.

1440 Rosinski, J., Nagamoto, C. T., and Zhou, M. Y.: Ice-forming nuclei over the East China Sea,  
1441 *Atmos. Res.*, 36, 95–105, [https://doi.org/10.1016/0169-8095\(94\)00029-D](https://doi.org/10.1016/0169-8095(94)00029-D), 1995.

1442 Schill, G. P. and Tolbert, M. A.: Heterogeneous ice nucleation on simulated sea-spray aerosol  
1443 using Raman microscopy, *J. Phys. Chem. C*, 118, 29234–29241,  
1444 <https://doi.org/10.1021/jp505379j>, 2014.

1445 Song, Y., Qiao, F., Liu, J., Shu, Q., Bao, Y., Wei, M., and Song, Z.: Effects of sea spray on large-  
1446 scale climatic features over the Southern Ocean, *J. Clim.*, 35, 4645–4663,  
1447 <https://doi.org/10.1175/JCLI-D-21-0608.1>, 2022.

1448 Stein, A. F., Draxler, R. R., Rolph, G. D., Stunder, B. J. B., Cohen, M. D., and Ngan, F.: NOAA' s  
1449 HYSPLIT atmospheric transport and dispersion modeling system, *Bull. Am. Meteorol. Soc.*, 96,  
1450 2059–2077, <https://doi.org/10.1175/BAMS-D-14-00110.1>, 2015.

1451 Su, B., Wang, T., Zhang, G., Liang, Y., Lv, C., Hu, Y., Li, L., Zhou, Z., Wang, X., and Bi, X.: A review  
1452 of atmospheric aging of sea spray aerosols: Potential factors affecting chloride depletion,  
1453 *Atmos. Environ.*, 290, 1–24, <https://doi.org/10.1016/j.atmosenv.2022.119365>, 2022.

1454 Tang, M., Cziczo, D. J., and Grassian, V. H.: Interactions of water with mineral dust aerosol:  
1455 water adsorption, hygroscopicity, cloud condensation, and ice nucleation, *Chem. Rev.*, 116,  
1456 4205–4259, <https://doi.org/10.1021/acs.chemrev.5b00529>, 2016.

1457 Tang, M. J., Schuster, G., and Crowley, J. N.: Heterogeneous reaction of N<sub>2</sub>O<sub>5</sub> with illite and  
1458 Arizona test dust particles, *Atmos. Chem. Phys.*, 14, 245–254, <https://doi.org/10.5194/acp-14-245-2014>, 2014.

1460 Tomlin, J. M., Jankowski, K. A., Veghte, D. P., China, S., Wang, P., Fraund, M., Weis, J., Zheng,  
1461 G., Wang, Y., Rivera-Adorno, F., Raveh-Rubin, S., Knopf, D. A., Wang, J., Gilles, M. K., Moffet,  
1462 R. C., and Laskin, A.: Impact of dry intrusion events on the composition and mixing state of  
1463 particles during the winter Aerosol and Cloud Experiment in the Eastern North Atlantic (ACE-  
1464 ENA), *Atmos. Chem. Phys.*, 21, 18123–18146, <https://doi.org/10.5194/acp-21-18123-2021>,  
1465 2021.

1466 Tomlin, J. M., Weis, J., Veghte, D. P., China, S., Fraund, M., He, Q., Reicher, N., Li, C., Jankowski,  
1467 K. A., Rivera-Adorno, F. A., Morales, A. C., Rudich, Y., Moffet, R. C., Gilles, M. K., and Laskin, A.:  
1468 Chemical composition and morphological analysis of atmospheric particles from an intensive  
1469 bonfire burning festival, *Environ. Sci.: Atmos.*, 2, 616–633,  
1470 <https://doi.org/10.1039/D2EA00037G>, 2022.

1471 Vali, G.: Quantitative evaluation of experimental results on the heterogeneous freezing  
1472 nucleation of supercooled liquids, *J. Atmos. Sci.*, 28, 402–409, [https://doi.org/10.1175/1520-0469\(1971\)028<0402:QEOERA>2.0.CO;2](https://doi.org/10.1175/1520-0469(1971)028<0402:QEOERA>2.0.CO;2), 1971.

1474 Wagner, R., Kaufmann, J., Möhler, O., Saathoff, H., Schnaiter, M., Ullrich, R., and Leisner, T.:  
1475 Heterogeneous ice nucleation ability of NaCl and sea salt aerosol particles at cirrus  
1476 temperatures, *J. Geophys. Res.: Atmos.*, 123, 2841–2860,  
1477 <https://doi.org/10.1002/2017JD027864>, 2018.

1478 Wang, B. and Knopf, D. A.: Heterogeneous ice nucleation on particles composed of humic-  
1479 like substances impacted by O<sub>3</sub>, *J. Geophys. Res.: Atmos.*, 116, 1–14,  
1480 <https://doi.org/10.1029/2010JD014964>, 2011.

1481 Wang, B., Laskin, A., Roedel, T., Gilles, M. K., Moffet, R. C., Tivanski, A. V., and Knopf, D. A.:  
1482 Heterogeneous ice nucleation and water uptake by field-collected atmospheric particles  
1483 below 273 K, *J. Geophys. Res.: Atmos.*, 117, 1–15, <https://doi.org/10.1029/2012JD017446>,  
1484 2012a.

1485 Wang, B., Lambe, A. T., Massoli, P., Onasch, T. B., Davidovits, P., Worsnop, D. R., and Knopf, D.  
1486 A.: The deposition ice nucleation and immersion freezing potential of amorphous secondary  
1487 organic aerosol: Pathways for ice and mixed-phase cloud formation, *J. Geophys. Res.: Atmos.*,  
1488 117, 1–12, <https://doi.org/10.1029/2012JD018063>, 2012b.

1489 Wang, B., O'Brien, R. E., Kelly, S. T., Shilling, J. E., Moffet, R. C., Gilles, M. K., and Laskin, A.:  
1490 Reactivity of liquid and semisolid secondary organic carbon with chloride and nitrate in  
1491 atmospheric aerosols, *J. Phys. Chem. A*, 119, 4498–4508, <https://doi.org/10.1021/jp510336q>,  
1492 2015.

1493 Wang, B., Harder, T. H., Kelly, S. T., Piens, D. S., China, S., Kovarik, L., Keiluweit, M., Arey, B. W.,  
1494 Gilles, M. K., and Laskin, A.: Airborne soil organic particles generated by precipitation, *Nat.*  
1495 *Geosci.*, 9, 433–437, <https://doi.org/10.1038/ngeo2705>, 2016a.

1496 Wang, B., Knopf, D. A., China, S., Arey, B. W., Harder, T. H., Gilles, M. K., and Laskin, A.: Direct  
1497 observation of ice nucleation events on individual atmospheric particles, *Phys. Chem. Chem.*  
1498 *Phys.*, 18, 29721–29731, <https://doi.org/10.1039/C6CP05253C>, 2016b.

1499 Welti, A., Lüönd, F., Stetzer, O., and Lohmann, U.: Influence of particle size on the ice  
1500 nucleating ability of mineral dusts, *Atmos. Chem. Phys.*, 9, 6705–6715,  
1501 <https://doi.org/10.5194/acp-9-6705-2009>, 2009.

1502 Welti, A., Müller, K., Fleming, Z. L., and Stratmann, F.: Concentration and variability of ice nuclei  
1503 in the subtropical maritime boundary layer, *Atmos. Chem. Phys.*, 18, 5307–5320,  
1504 <https://doi.org/10/gdggbd>, 2018.

1505 Welti, A., Bigg, E. K., DeMott, P. J., Gong, X., Hartmann, M., Harvey, M., Henning, S., Herenz,  
1506 P., Hill, T. C. J., Hornblow, B., Leck, C., Löffler, M., McCluskey, C. S., Rauker, A. M., Schmale, J.,  
1507 Tatzelt, C., van Pinxteren, M., and Stratmann, F.: Ship-based measurements of ice nuclei

1508 concentrations over the Arctic, Atlantic, Pacific and Southern oceans, *Atmos. Chem. Phys.*, 20,  
1509 15191–15206, <https://doi.org/10.5194/acp-20-15191-2020>, 2020.

1510 Wilson, T. W., Ladino, L. A., Alpert, P. A., Breckels, M. N., Brooks, I. M., Browse, J., Burrows, S.  
1511 M., Carslaw, K. S., Huffman, J. A., Judd, C., Kilhau, W. P., Mason, R. H., McFiggans, G., Miller,  
1512 L. A., Nájera, J. J., Polishchuk, E., Rae, S., Schiller, C. L., Si, M., Temprado, J. V., Whale, T. F.,  
1513 Wong, J. P. S., Wurl, O., Yakobi-Hancock, J. D., Abbatt, J. P. D., Aller, J. Y., Bertram, A. K., Knopf,  
1514 D. A., and Murray, B. J.: A marine biogenic source of atmospheric ice-nucleating particles,  
1515 *Nature*, 525, 234–238, <https://doi.org/10.1038/nature14986>, 2015.

1516 Xiao, H. S., Dong, J. L., Wang, L. Y., Zhao, L. J., Wang, F., and Zhang, Y. H.: Spatially resolved  
1517 micro-Raman observation on the phase separation of effloresced sea salt droplets, *Environ.*  
1518 *Sci. Technol.*, 42, 8698–8702, <https://doi.org/10.1021/es801181f>, 2008.

1519 Yakobi-Hancock, J. D., Ladino, L. A., and Abbatt, J. P. D.: Feldspar minerals as efficient  
1520 deposition ice nuclei, *Atmos. Chem. Phys.*, 13, 11175–11185, [https://doi.org/10.5194/acp-13-](https://doi.org/10.5194/acp-13-11175-2013)  
1521 11175-2013, 2013.

1522 Yan, J., Jung, J., Zhang, M., Bianchi, F., Tham, Y. J., Xu, S., Lin, Q., Zhao, S., Li, L., and Chen, L.:  
1523 Uptake selectivity of methanesulfonic acid (MSA) on fine particles over polynya regions of the  
1524 Ross Sea, Antarctica, *Atmos. Chem. Phys.*, 20, 3259–3271, [https://doi.org/10.5194/acp-20-](https://doi.org/10.5194/acp-20-3259-2020)  
1525 3259-2020, 2020.

1526 Yao, Y., Curtis, J. H., Ching, J., Zheng, Z., and Riemer, N.: Quantifying the effects of mixing state  
1527 on aerosol optical properties, *Atmos. Chem. Phys.*, 22, 9265–9282, [https://doi.org/10.5194/acp-22-](https://doi.org/10.5194/acp-22-9265-2022)  
1528 9265-2022, 2022.

1529 Zhang, M., Chen, L., Xu, G., Lin, Q., and Liang, M.: Linking phytoplankton activity in polynyas  
1530 and sulfur aerosols over Zhongshan Station, East Antarctica, *J. Atmos. Sci.*, 72, 4629–4642,  
1531 <https://doi.org/10.1175/JAS-D-15-0094.1>, 2015.

1532